Quaternary Science Reviews 105 (2014) 66–85

Contents lists available at ScienceDirect

Quaternary Science Reviews

journal homepage: www.elsevier.com/locate/quascirev

Quaternary landscape development, alluvial fan chronology and erosion of the Mecca Hills at the southern end of the San Andreas Fault zone

Harrison J. Gray [a, b, *], Lewis A. Owen [b], Craig Dietsch [b], Richard A. Beck [c], Marc A. Caffee [d], Robert C. Finkel [e], Shannon A. Mahan [a]

[a] U.S. Geological Survey, Box 25046 MS 974, Denver, CO 80225, USA
[b] Department of Geology, University of Cincinnati, Cincinnati, OH 45221, USA
[c] Department of Geography, University of Cincinnati, Cincinnati, OH 45221, USA
[d] Department of Physics/PRIME Laboratory, Purdue University, West Lafayette, IN 47906, USA
[e] Department of Earth and Planetary Sciences, University of California, Berkeley, CA 94720, USA

ARTICLE INFO

Article history:
Received 8 February 2014
Received in revised form
14 August 2014
Accepted 5 September 2014
Available online

Keywords:
Terrestrial cosmogenic nuclides
Beryllium-10
Surface exposure dating
Mecca Hills
San Andreas Fault

ABSTRACT

Quantitative geomorphic analysis combined with cosmogenic nuclide ^{10}Be-based geochronology and denudation rates have been used to further the understanding of the Quaternary landscape development of the Mecca Hills, a zone of transpressional uplift along the southern end of the San Andreas Fault, in southern California. The similar timing of convergent uplifts along the San Andreas Fault with the initiation of the sub-parallel San Jacinto Fault suggest a possible link between the two tectonic events. The ages of alluvial fans and the rates of catchment-wide denudation have been integrated to assess the relative influence of climate and tectonic uplift on the development of catchments within the Mecca Hills. Ages for major geomorphic surfaces based on ^{10}Be surface exposure dating of boulders and ^{10}Be depth profiles define the timing of surface stabilization to 2.6 +5.6/−1.3 ka (Qyf1 surface), 67.2 ± 5.3 ka (Qvof2 surface), and 280 ± 24 ka (Qvof1 surface). Comparison of ^{10}Be measurements from active channel deposits (Qac) and fluvial terraces (Qt) illustrate a complex history of erosion, sediment storage, and sediment transport in this environment. Beryllium-10 catchment-wide denudation rates range from 19.9 ± 3.2 to 149 ± 22.5 m/Ma and demonstrate strong correlations with mean catchment slope and with total active fault length normalized by catchment area. The lack of strong correlation with other geomorphic variables suggests that tectonic uplift and rock weakening have the greatest control. The currently measured topography and denudation rates across the Mecca Hills may be most consistent with a model of radial topographic growth in contrast to a model based on the rapid uplift and advection of crust.

Published by Elsevier Ltd.

1. Introduction

Understanding the Quaternary evolution of fault systems in tectonically active environments is essential for evaluating both modern seismic hazard and the long-term tectonic processes of plate boundaries. Southern California is one such environment where the San Andreas Fault acts in concert with other major strike slip fault systems to form a dynamic and complex system (Fig. 1; Matti and Morton, 1993; Janecke et al., 2010; Dorsey et al., 2012). Part of this complexity is expressed by the interaction of the San Andreas Fault and San Jacinto Fault which have had a strong interplay in slip rates (Bennett et al., 2004; Janecke et al., 2010) leading to questions of how strain is partitioned between the two structures. Interestingly, the southern San Andreas Fault is host to the Durmid, Indio, and Mecca Hills which represent “restraining bends” where strike slip motion is converted into compression throughout the Quaternary (Sylvester and Smith, 1976; Bilham and Williams, 1985). The presence of the Bishop Tuff (Ware, 1958; Merriam and Bischoff, 1975; Rymer, 1991) define the uplift of the Mecca Hills to sometime prior to 767.1 ± 0.9 ka (Izett and Naeser, 1976; Reid and Coath, 2000; Crowley et al., 2007) but not earlier than 1.2–1.5 Ma (McNabb et al., 2013). The timing of uplift of the Mecca Hills, and possibly the

* Corresponding author. U.S. Geological Survey, Box 25046 MS 974, Denver, CO 80225, USA. Tel.: +1 720 353 8690.
E-mail address: harrison.gray@colorado.edu (H.J. Gray).

http://dx.doi.org/10.1016/j.quascirev.2014.09.009
0277-3791/Published by Elsevier Ltd.

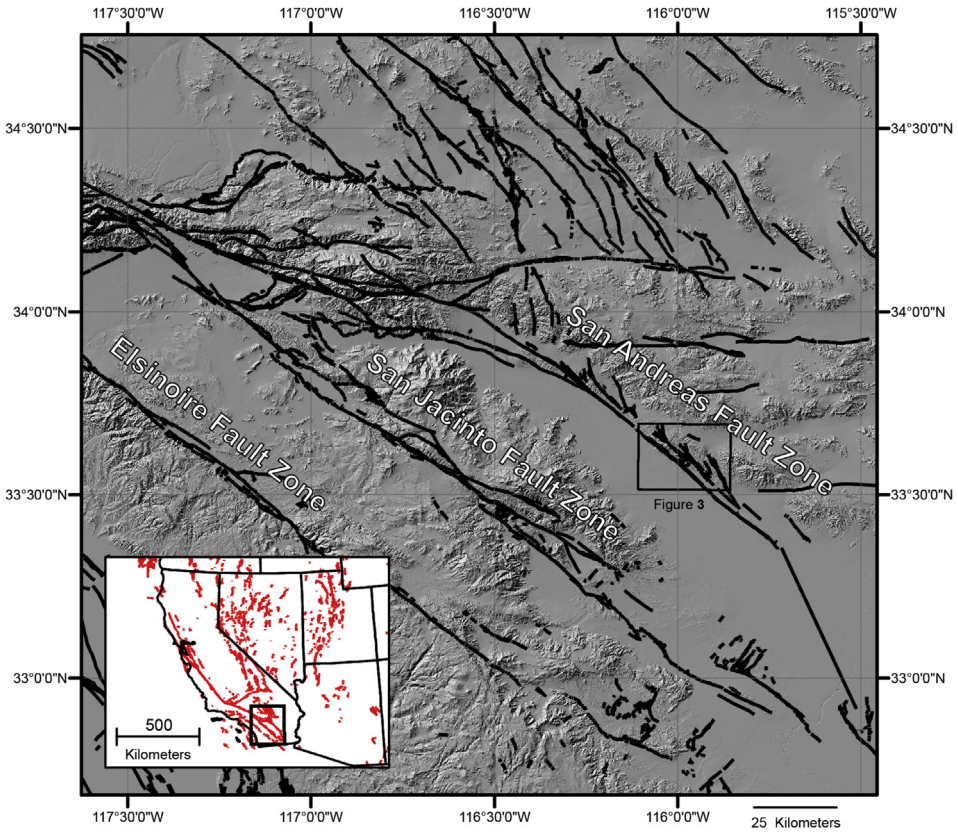

Fig. 1. Location of the Mecca Hills in southern California showing major faults. Background image is a hillshade derived from a 1-arc second digital elevation model (DEM) from the U.S. Geological Survey (USGS) National Elevation Dataset. Fault lines are sourced from the USGS fault data repository (Petersen et al., 2008).

timing of uplift of the Durmid and Indio Hills (Bilham and Williams, 1985), correlates with the initiation of the San Jacinto Fault. Contemporaneous origin of the restraining bends with the San Jacinto Fault initiation suggests that a significant change in the stress field on the southern San Andreas Fault occurred with San Jacinto Fault initiation which shifted motion from strike slip towards convergence (Fattaruso et al., 2013). Alternatively, the restraining bends observed along the southern San Andreas Fault may instead represent local fault plane heterogeneities or "structural knots" (Hilley and Arrowsmith, 2008) which have generated the uplifts. These two forms of restraining bend development can be distinguished by the spatial patterns of uplift rate (Fig. 2). In this paper, we conduct a quantitative geomorphic study of the Mecca Hills to determine if the observed spatial patterns of uplift and erosion are consistent with local fault plane heterogeneity or a possible reorganization of strain on the San Andreas Fault. Our approach utilizes: (1) geomorphic mapping with an emphasis on alluvial fans; (2) ^{10}Be geochronology to assess ages and fluvial incision rates of geomorphic surfaces; and (3) measurement of ^{10}Be in sediment to quantify catchment averaged rates of denudation.

In regions where reverse faulting is a significant component of slip partitioning, the record of vertical fault motion can be obscured by long-term denudation or a lack of fault surface expression (Aydin et al., 1992; Philip and Meghraoui, 1983). The long-term record of fault uplift, however, is expressed as elevated topography which in turn produces denudation rates in a pattern similar to the distribution of fault uplift rates at the watershed scale (Cyr et al., 2010; Binnie et al., 2008; Gudmundsdottir et al., 2013). One method to evaluate the spatial patterns of uplift and denudation is through the use of quantitatively defined landscape evolution models that provide useful limits for evaluating slip partitioning in tectonically active regions with a significant component of reverse faulting (Wobus et al., 2006; Kirby et al., 2008; Gudmundsdottir et al., 2013). However, the vertical motions of faults in the Mecca Hills are difficult to determine with traditional paleoseismic methods owing to the lack of preserved surface expression and depositionally complex stratigraphy. Instead, we construct and test two endmember landscape evolution models as working hypotheses to evaluate uplift patterns.

Our endmember models are based on previous research on the topographic development of transpressive "restraining bends" in strike slip tectonic systems (Fig. 2; Cunningham and Mann, 2007; Mann, 2007). The primary difference in the models is the location of the focal point of maximum uplift which plays a key role in the development of topography (Fig. 2; Anderson, 1994; Cowgill et al., 2004a; Hilley and Arrowsmith, 2008). Model 1 is developed from previous work in the Mecca Hills and from theoretical and analog models of restraining bend development (Sylvester and Smith, 1976; Woodcock and Fischer, 1986; McClay and Bonora, 2001). Conceptually, the focal point of maximum uplift is located in the center of the restraining bend and tapers toward the edges creating a domal pattern of uplift rate. Model 2 is constructed from research demonstrating that the topographic expression of restraining bends occurs from a focal point of uplift followed by advection of material (Fig. 2; Anderson, 1994; Bürgmann et al., 1994; Hilley and Arrowsmith, 2008). Note that restraining bends obey a spectrum of uplift styles depending on fault geometry and principal stress orientations (Cowgill et al., 2004; Cunningham, 2007; Mann, 2007). The data presented in our study favor Model 1 and seem to exclude the possibility of Model 2.

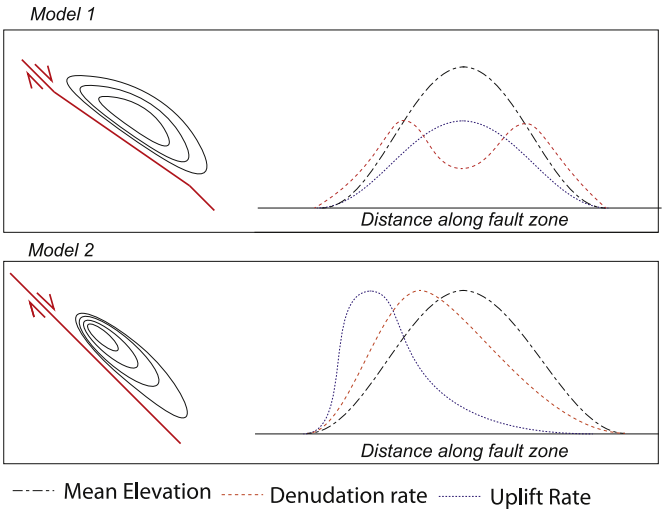

Fig. 2. Two potential models describing the topographic evolution of the Mecca Hills. Red line indicates fault trace. Black lines are contours of surface uplift rate. Model 1 is based on radial topographic growth from a central point which spreads outward (Patt, 2000). Model 2 is based on the presence of a potential "structural knot" (Hilley and Arrowsmith, 2008) which uplifts topography at a focal point which is advected and eroded with progressive horizontal offset. Graphs show the predicted along-fault pattern of elevation, uplift rate, and denudation rate. (For interpretation of the references to colour in this figure legend, the reader is referred to the web version of this article.)

2. Regional setting

The Coachella Valley is a northern extension of the Salton Trough, a pull-apart basin tied to rifting in the Gulf of California (Axen and Fletcher, 1998). The San Andreas Fault along this segment exhibits a "sawtooth" geometry in map view consisting of low-relief strike-slip segments bounded by high-relief transpressive segments (Sylvester and Smith, 1976; Sylvester, 1988; Bilham and Williams, 1985; Spotila et al., 2007, Fig. 1). The transpressive segments, known geographically as the Indio, Mecca, and Durmid Hills, demonstrate significant deformation and uplift (Dibblee, 1954; Sylvester and Smith, 1976). Of these transpressive segments, the Mecca Hills seem to demonstrate the greatest cumulative uplift because of the exhumation of the underlying bedrock from below the basin fill, presence of significant folding, and laterally more extensive landscape dissection by rivers (Sylvester and Smith, 1976). Because the Bishop Tuff is present in the deformed stratigraphy of the Mecca Hills (Rymer, 1991), the hills potentially provide a record of deformation since 767.1 ± 0.9 ka. In addition, the Mecca Hills has several geomorphic indicators of rapid landscape change since the onset of uplift at 740 ka (Rymer, 1991) including high relief, steep hillslopes, slot canyons, and abandonment of geomorphic surfaces such as alluvial fan terraces.

The Mecca Hills were originally mapped at a regional scale by Dibblee (1954) and at a local scale by Ware (1958). The main stratigraphic units were defined (from oldest to youngest) as the Mecca Formation, the Palm Spring Formation, and the Ocotillo Conglomerate. These units are composed of a sequence of weakly lithified to unlithified, silicilastic, non-marine deltaic and lacustrine deposits capped by fanglomerates (Sylvester and Smith, 1976). Discovery of vertebrate fossils in the Mecca Hills by Hays (1957) and Ware (1958) indicate a late Cenozoic age for the Palm Spring Formation. Detailed mapping and stratigraphic work by Sheridan and Weldon (1994) and Boley et al. (1994) built on and expanded the mapping of Sylvester and Smith (1976), and added to the paleomagnetic work of Chang et al. (1987). Discovery of the Bishop Tuff within the Palm Spring Formation by Ware (1958) and its chemical analysis by Merriam and Bischoff (1975) provided further proof of the late Cenozoic age for these formations. The structural geology of the Mecca Hills was studied by Sylvester and Smith (1976). They proposed a model of partitioned transpression, and designated the principal high-angle faults in the core of the Mecca Hills as a 'palm tree' structure. This seminal work provided the foundation for future models of transpressional deformation (Fossen and Tikoff, 1998). Sheridan and Weldon (1992) reinterpreted the structural geology, suggesting an alternate model of compression involving upward and inward motion of the sedimentary units by cataclastic flow against a bedrock buttress. Patt's (2000) analysis of the Quaternary geology of the Mecca Hills represented the first modern geomorphic analysis of the region and interpreted the distribution of drainage networks and topography as that of an outwardly growing young mountain range.

3. Methods

3.1. Geomorphic mapping of alluvial fan surfaces

We follow the mapping, unit descriptions, and conventions of Patt (2000; Fig. 3; Table 1), who utilized and slightly modified the relative weathering methodology proposed by Burke and Birkeland (1979) and McFadden et al. (1989). Patt (2000) developed the alluvial stratigraphic sequence using the following criteria: (1) number, pitting, splitting, and relief of boulders; (2) degree of rock varnish and extent of desert pavement development; (3) percent vegetation cover and plant diversity; and (4) soil development and solum depth. Our numbering scheme for geomorphic surfaces was adopted from the designations of Patt (2000) who used a scheme loosely based on regional alluvial chronologies (Bull, 1987; McFadden et al., 1989; Wells et al., 1990; Hooke and Dorn, 1992). Based on the relative weathering system, Patt (2000) designated the oldest alluvial surface as Qvof1 and named the next youngest surface as Qvof2. Patt (2000) designated the most recently abandoned alluvial fan surface as Qyf1 and fluvial fill terraces as Qt1 and named the active alluvial fan deposits as Qac.

Fieldwork was undertaken to corroborate the mapping of Patt (2000) and to collect samples for ^{10}Be geochronology. Digital mapping was performed remotely using ArcGIS 10.1 Education Edition on 10 m pixel digital elevation models from the National Elevation Dataset (Gesch et al., 2002; Gesch, 2007) and aerial photography from CalAtlas (State of California (2013)). We limited our interpretation of the continuous extent of surfaces sampled for geochronology to avoid over extrapolation of age results. The regional geology adapted from Patt (2000) is shown in Fig. 3 with geomorphic Qvof1, Qvof2, and Qyf1 surfaces based on relative weathering correlation, and demonstrates the extent of geomorphic surfaces beyond our sampled region. Our detailed digital mapping results are presented in Figs. 4 and 5. Faults within the Mecca Hills were not mapped in this study; we instead refer to data from the USGS fault and fold database (U.S. Geological Survey and California Geological Survey, 2013), Patt (2000), and structures from Sylvester and Smith (1976) (Figs. 3 and 4). Typical views of the mapped geomorphic surfaces are presented in Fig. 6.

3.2. ^{10}Be methods

Samples were crushed and sieved to a 250–500 μm particle size and treated with aqua regia to remove carbonates and organic

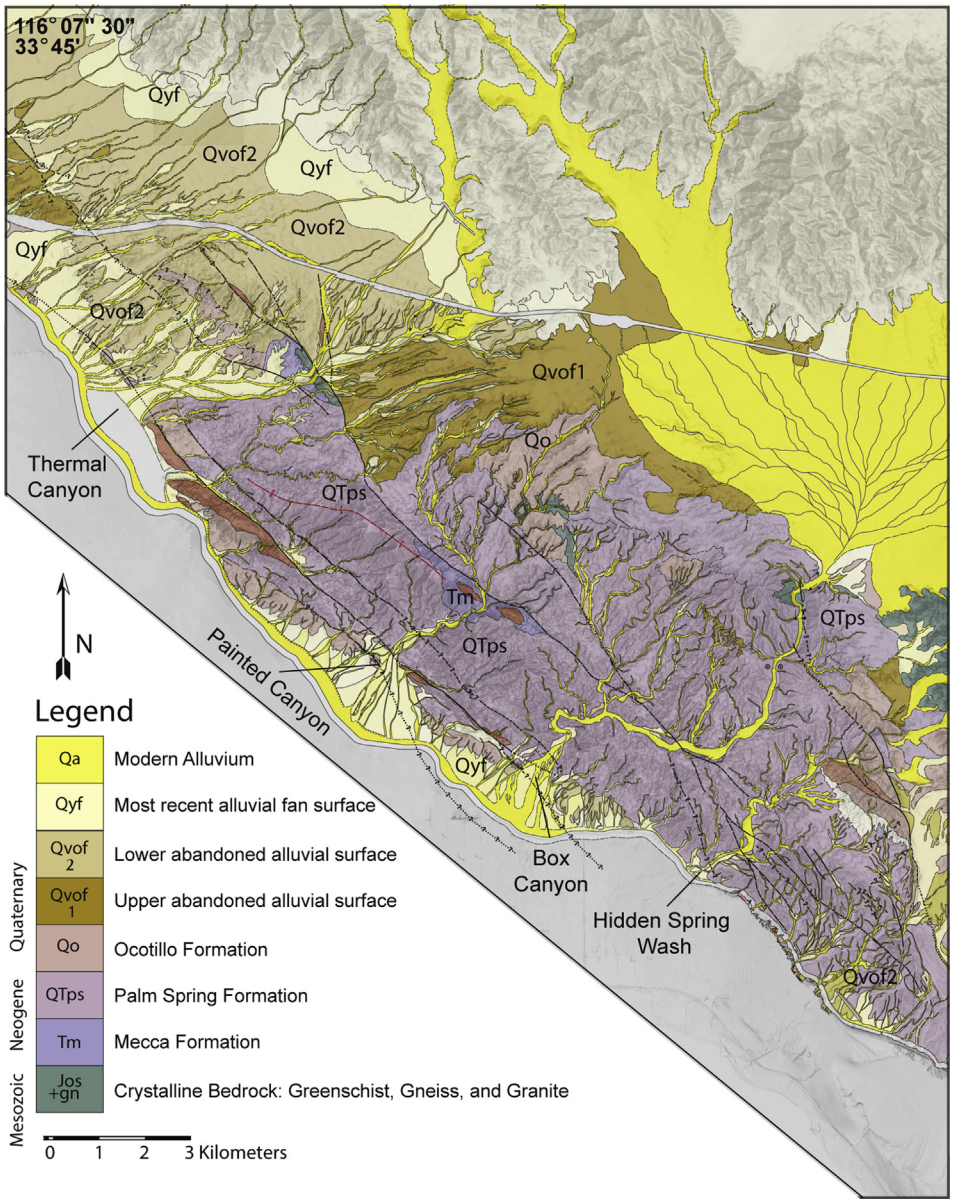

Fig. 3. The Mecca Hills showing surficial geology and major structures adapted from Patt (2000). Note widespread presence of surfaces Qvof1, Qvof2, and Qyf.

material, then placed in a 24-h 5% hydrofluoric solution to etch, dissolve, and disintegrate non-quartz minerals. The remaining sample was rinsed and agitated with a high velocity 10% Lauryl Amine and CO_2 spray to pulverize and evacuate feldspathic minerals. Samples were then subjected to further quartz purification using a Frantz Magnetic Separator and lithium sodiumpolytungstate. The chemical preparation of quartz follows the method developed by Nishiizumi et al. (1993). The resulting $Be(OH)_2$ gel of each sample was dried and combusted at 700 °C before being mixed with Nb powder and loaded in cathode targets for accelerator mass spectrometry (AMS) at PRIME lab at Purdue University and at the Lawrence Livermore National Laboratory to determine $^{10}Be/^{9}Be$ ratios. Ages were derived from AMS-determined ^{10}Be concentrations using the online CRONUS calculator (Balco et al., 2008). Age results including various models for age determinations are present in Table 2 following reporting methods suggested by Frankel et al. (2010). Our preferred age is obtained with the time-dependent scaling models of Lal (1991) and Stone (2000) in order to make our chronologies consistent with other age data from the region (Owen et al., 2014). The choice of scaling model does not vary the age significantly enough to alter our interpretations (Table 2).

3.3. Surface exposure ages

Surface exposure ages of geomorphic units/surfaces within the Mecca Hills were determined by ^{10}Be chronology (Table 2). The Qvof1 and Qvof2 surfaces were targeted for ^{10}Be geochronology because they are significant in the Mecca Hills alluvial stratigraphy (Patt, 2000) and allow us to infer the patterns of tectonic uplift. The Qyf1 and Qt1 surfaces were targeted to examine levels of inheritance in the system and to check if the landscape response to climate change, such as the Marine Isotope Stage (MIS) 1/2 transition, resulted in the deposition of these units. Samples on major

Table 1
Geomorphic Surface descriptions.

Surface name	Mean sampled elevation (m a.s.l.)	Description of surface
Qvof1	550	This is the highest surface in the alluvial stratigraphy and is dominantly present in the northeastern side of the Mecca Hills. It demonstrates an extremely well developed desert pavement with little bar and swale morphology. Polymictic granite and metamorphic sand to cobble lithology with infrequent boulders. Significant carbonate development and ventifacts are present. Vegetation density is very low and displays greater diversity than other surfaces in the Mecca Hills.
Qvof2	110	This surface is the most prominent surface in the Northwestern Mecca Hills northwest of Thermal Canyon (Fig 2). Desert pavement development is weaker than Qvof1 yet boulders at the surface have significant rock varnish and are weathered. Remnant bar and swale features are present. Carbonate soil development is present but thinner than Qvof1. Vegetation density is low and less diverse than Qvof1
Qyf1	81	This is the most recent episode of alluvial fan deposition in the Mecca Hills. Little to no desert pavement or varnish on boulders. Boulders are not weathered and intact and frequent on surfaces. Lithology is identical to other alluvial units. Sand to cobble clasts size. Bar and swale features present. Vegetation is sparse and not diverse.
Qt1	156	Very similar to Qyf1 except appears morphology as fluvial terraces as opposed to alluvial fans. Lithology varies between granite/gneiss and schist dominated end members depending on location.
Qac	57	Active channel deposits that are reactivated on occurrence of flash flooding. Imbricated boulders and cobbles present. Vegetation is denser and more diverse relative to other surfaces. Lithology is a mix of granite, gneiss, and rarely schist. Beryllium-10 concentrations assumed to be entirely inheritance

geomorphic surfaces were collected from boulders that demonstrated minimal weathering and erosion as evident from a strong desert varnish and a lack of physical weathering features, such as fracturing and disintegration. We further restricted our sampling to boulders which were well inset into the ground, with no possibility for toppling, and boulders which were located away from topographic lows and/or hillslopes (Fig. 6). Samples were collected by hammering off 1–5 cm-thick layers from horizontal boulder tops (avoiding the sides) using a hammer and chisel; sample masses ranged from 300 to 1000 g.

Exposure ages were grouped based on mapped geomorphic surfaces and analyzed using a normal kernel probability density estimate (NKDE; Fig. 7) and a mean square weighted deviation (MSWD) test (McDougall and Harrison, 1988; Powell et al., 2002; Streule et al., 2009). Surface exposure ages are the weighted mean of all ages passing the MSWD criteria; the uncertainty is expressed as 1-σ values of those ages. For surfaces whose ages do not pass the MSWD test, the surface age and uncertainty is the weighted mean and the 1-σ standard deviation of all ages from that surface. The NKDE analysis, also known as a probability distribution function plot of the sum of the individual Gaussian distributions, quantifies the scattering of boulder surface exposure ages for a given geomorphic surface. Curves were produced using Camelplot MATLAB code developed by Balco (2009). We assumed zero erosion for all surface exposure age calculations. We calculated fluvial incision rates into surfaces proximal to the San Andreas Fault by using the mean boulder exposure age of the incised surfaces and the average elevation of the surfaces above the channel. The average elevation above the channel was determined in the field by multiple measurements using an inclinometer and measuring tape. The average was calculated and measurement stopped when the average did not change significantly with further data. The calculated incision rates are supplemented with a tectonic uplift rate of 1.8 mm/yr near Painted Canyon based on stratigraphic relations from McNabb and Dorsey (2012).

3.4. Depth profiles

For the Qvof1, Qvof2, and Qyf1 surfaces, surface exposure ages were also determined by ^{10}Be concentration in depth profiles (Fig. 8, Tables 3 and 4). Samples were collected at equal (~20 cm) depth intervals below the surface from artificially dug 1.5–2 m deep pits or natural exposures that were enlarged to a depth of approximately 1 m, (Table 3). The ^{10}Be concentrations were modeled using depth profile simulator MATLAB code developed by Hidy et al. (2010).

3.5. Catchment-wide denudation rates

Catchment-wide denudation rates for the Mecca Hills were determined using ^{10}Be concentrations in active-channel alluvial sediments (Lal and Arnold, 1985; Brown et al., 1995; Bierman and Steig, 1996; Granger et al., 1996, Fig. 4, Table 5). Samples were collected throughout the major drainage networks but with a focus on Painted, Thermal, and Box Canyons (Fig. 3). Approximately ~1 kg of sediment from the trace of the active channel was collected in the upper, middle, and lower reaches of each sampled drainage system. One sample, MH-HG-ER1, was collected at Red Canyon approximately 7500 m distance along the San Andreas Fault (Fig. 9), but did not yield enough quartz for measurement. Upstream catchments of sample locations were delineated and extracted using standard flow-routing algorithms in ArcGIS 10.0 on USGS National Elevation Dataset DEMs (nationalmap.gov) and compared with USGS topographic maps during field work in 2012. Catchment-wide ^{10}Be production rates were calculated using the methods and MATLAB (2009) code of Dortch et al. (2011). Individual ^{10}Be production rates (Lal, 1991) were calculated on a pixel-by-pixel basis using the scaling factors of Stone (2000) and averaged over the entire catchment. Production rates were corrected for topographic shielding on a pixel-by-pixel basis by calculating the maximum angle to the horizon and using this as the shielding estimate (see Dortch et al., 2011).

To test if the tectonic signal was dominant in controlling denudation rate, we examined correlations between variables thought to control catchment-wide denudation rates (von Blanckenburg, 2005; Portenga and Bierman, 2011) and the total mapped fault length divided by catchment area. This is in order to distinguish if a strong relationship between tectonic processes such as uplift or rock weakening exists or if a scaling of denudation rate with basin size was obscuring any tectonic control. We examined the geomorphic variables of mean basin slope, basin size, basin relief, basin elevation, and total length of mapped faults normalized by catchment area (Table 6, Fig. 10). Geomorphic variables were measured using ArcGIS 10.1 on National Elevation Dataset 10 m per

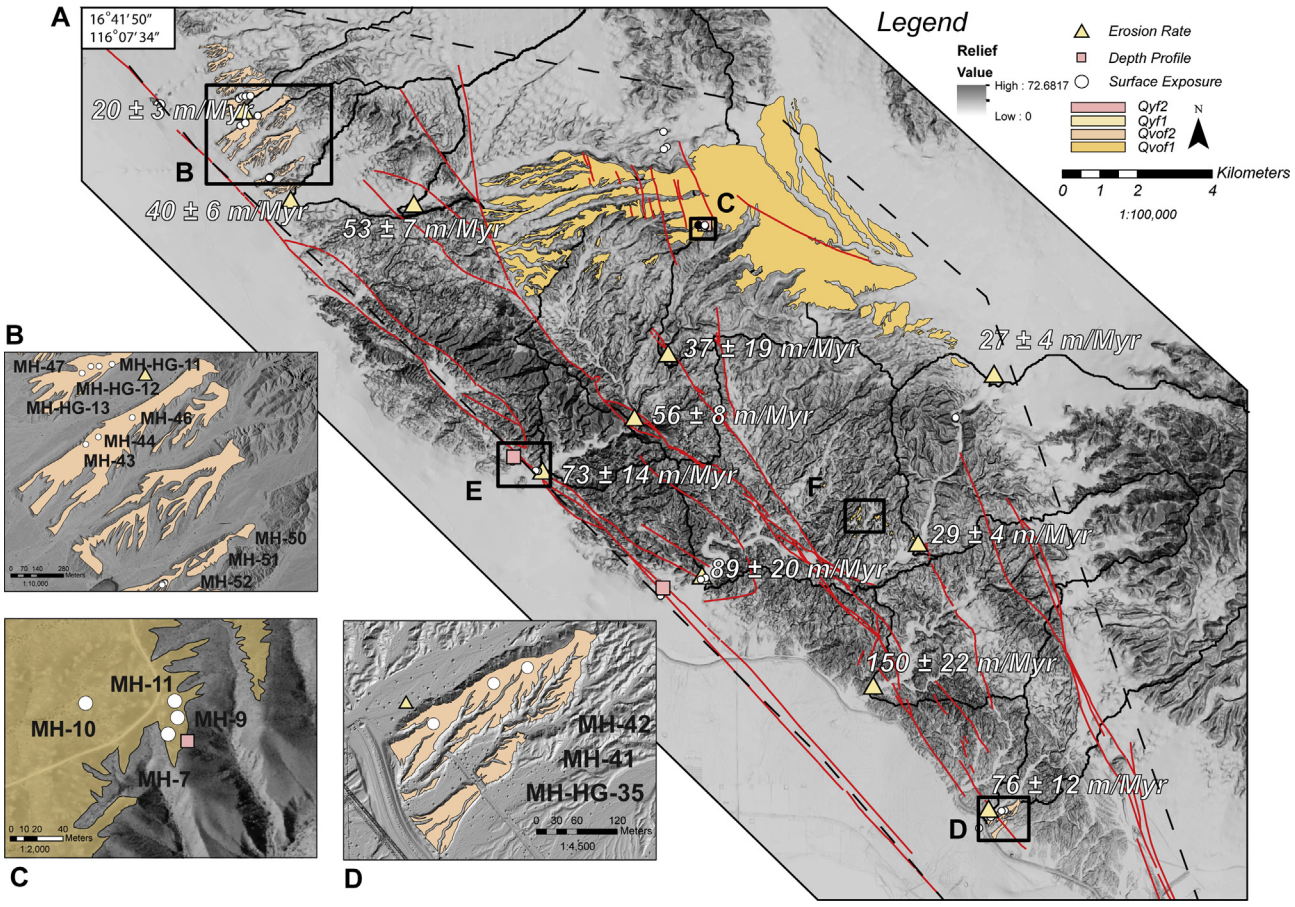

Fig. 4. (A) Overview of the geomorphology of the Mecca Hills, CA, including sample locations, geomorphic mapping, and denudation rate results. Background image is an overlay of a hillshade image derived from a 10 m per pixel DEM from the USGS National Elevation Dataset overlain with a range focal statistics raster to enhance topographic relief. Dark shades indicate higher local topographic relief. Fault lines are from the USGS fault and fold database. Dashed line indicates region used for swath profile in Fig. 11 (see text). (B–F) Insets of local scale mapping and locations of samples. Note that E and F refer to Figs. 5a and b. Hillshade in image insets is derived from the B4 LiDAR dataset (Bevis et al., 2005) and aerial imagery is obtained from CalAtlas (State of California (2013)).

pixel DEMS. Catchment relief was determined as maximum minus minimum elevations following Portenga and Bierman (2011). Total mapped fault length was determined from the USGS fault and fold database and measured using the measure tool in ArcGIS 10.1. This total fault length was divided by the catchment area and compared with the corresponding denudation rate. Regression of denudation rates versus geomorphic variables was conducted and presented in Figs. 9 and 10.

3.6. Landscape morphometrics

Catchment denudation rates were compared against the swath mean elevation and topographic relief, and tectonic uplift/fluvial incision rates determined from alluvial fan surface ages (Fig. 11) in order to test our two models against the data. To do so, it is necessary to distinguish the elevations due to tectonic deformation from those due to the regional slope such that swath profiles of the

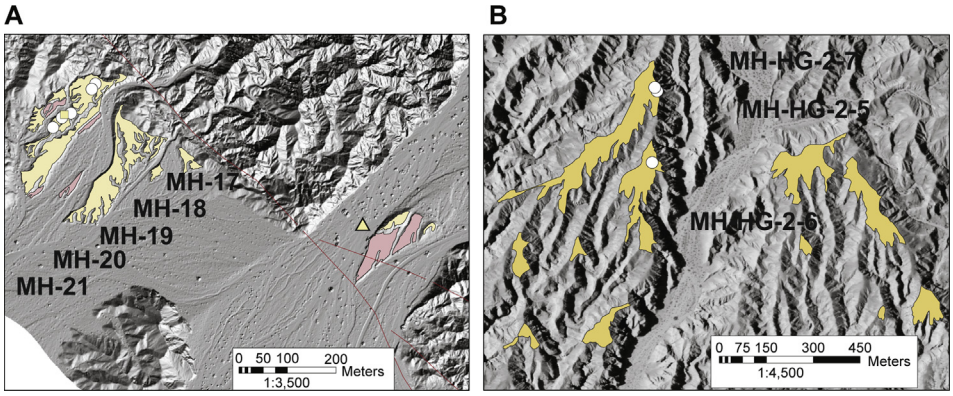

Fig. 5. Zoom-ins of insets in Fig. 4. See Fig. 4 for legend. The hillshade in A is illuminated from an azimuth of 135. Aerial imagery in B is obtained from CalAtlas (State of California (2013)).

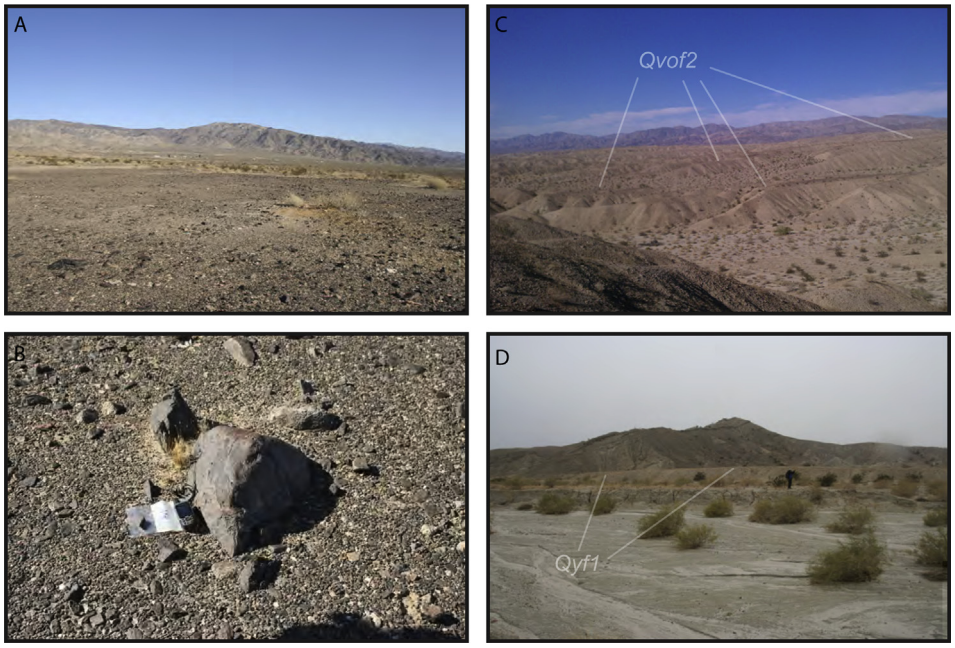

Fig. 6. Views of characteristic geomorphology of the Mecca Hills. (A) Surface Qvof1 displaying even surface with little to no bar and swale features (33.6579°N/115.9805°W, 540 m asl). Note dark color of surface. (B) Boulder from surface Qvof1 representative of boulders sampled for beryllium-10 surface exposure dating (33.6553°N/115.9832°W, 545 m asl). Note strong rock varnish and well developed desert pavement. (C) Surface Qvof2 looking northwestward from ridge north of Thermal Canyon (33.6724°N/116.0874°W, 108 m asl). Surface exhibits gently sloping flat surfaces above incised broad channels. (D) View of surface Qyf1 taken from incised channel looking towards sampling locations; (33.6075°N/116.0288°W, 97 m asl). Notice gently sloping gradient of upper surface and inset lower surface. Photographs taken by Suyoung Lee, used with permission.

topography are not inadvertently skewed towards values t higher elevation. The swath mean elevation and topographic relief were found using functions in ArcGIS 10 over an area defined by the slope breaks between the uplifted topography of the Mecca Hills and the background regional slope. We took the average gradient between the Indio and the Mecca Hills where uplift is thought to be minimal (Bilham and Williams, 1985) and subtracted from the elevations in the Mecca Hills DEM. The gradient was obtained along a river profile from 33.73023 °N/116.15134°W to 33.75123 °N/116.10929 °W. In addition, we subtracted the regional slope parallel to the northwest-to-southeast drainage towards the Salton Sea from the Mecca Hills DEM in order to remove the regional subsidence from the opening of the Salton Trough (Brothers et al., 2009). This gradient was obtained from the basin surface from 33.64913°N/116.12382 °W to 33.52317 °N/115.97264 °W. This produces a Mecca Hills DEM where the elevations distinct from the regional slopes can be compared with tectonic uplift rates and with denudation rates. By considering fluvial incision rates as a *first-order approximation* of rock uplift rates based on findings by Litchfield and Berryman (2006), we generated a "tectonic uplift" curve by plotting fluvial incision rates from boulder ages and a rock uplift rate of 1.8 mm/yr from McNabb and Dorsey (2012) (Fig. 11). We acknowledge that fluvial incision rates do not always follow rock uplift rates and often overestimate the actual rate of uplift by a factor of 1.5–5 (Litchfield and Berryman, 2006). However, we provide the data here as a first-order approximation for qualitative purposes.

4. Results

4.1. Geomorphic mapping

Geomorphic mapping of the Qvof1, Qvof2, and Qyf1 surfaces are presented in Figs. 4 and 5 with insets showing detailed mapping of sampling locations. The minor Qyf2 surface was mapped to differentiate it from the Qyf1 surface in the Painted Canyon study site (Fig. 5a). The Qvof1 surface demonstrates the greatest relative age based on our multi-parameter approach (Burke and Birkeland, 1976; McFadden et al., 1989; Patt, 2000). The Qvof1 surface is composed of polymictic granite (60–70%), gneiss (10–20%), and greenschist (10–20%). The sediment was probably derived from the nearby Little San Bernardino, Cottonwood, and Orocopia Mountains (Patt, 2000). All surface constituents have a well-developed desert pavement and rock varnish (5YR 2/1 to N2). Surface boulders are not common and when present are heavily pitted and often split; surface clasts are poorly sorted, subrounded to angular, and highly rubified. A stage 3–4 calcic horizon is present and the solum depth is 30 cm. Granitic boulders often appear completely decomposed. Some ventifacts are present on the geomorphic surface. Plant diversity is high relative to other alluvial surfaces and vegetation is sparse. In places, the surface slope of surface Qvof1 appears to be back-tilted from a presumably original southwesterly dip to an approximate east-northeast dip due to the uplift of the Mecca Hills. This can be seen from Highway 10 as the Mecca Hills is approached from the east.

The Qvof2 surface is less weathered than Qvof1 and is morphologically discontinuous (Fig. 4; Fig. 6). Desert pavement is less developed as indicated by the lighter brown varnish (5YR 3/4) and occasional clast layering at the surface. The lithology of the Qvof2 surface is very similar to the Qvof1 surface with clast composition approximately 60–70% granite, 10–20% gneiss and 10–20% greenschist. Boulders are moderately pitted and some are split with fresh faces; surface clasts have sporadic rubification, no ventification, and a weaker calcic horizon than the Qvof1 surface along with lower vegetation diversity.

The Qyf1 surface shows the youngest relative age of sampled surfaces in the Mecca Hills. A desert pavement has not yet developed and rock varnish is minimal with no rubification of clasts. There is no soil developed on this surface. Similar to the Qvof1 and Qvof2 surfaces, the lithology of the Qyf1 surface is dominantly granitic but also

Table 2
^{10}Be sample data and surface exposure ages for boulders.[e]

Sample name	Geomorphic unit	Rock type	Latitude °N	Longitude °W	Elevation (m)	Boulder size l/w/h (cm)	Thickness[c] (cm)	Quartz mass (g)	^{9}Be Carrier (g)
MH-7	Qvof1	Gneiss	33.6575	115.9805	540	80/45/25	5	14.395	0.9541
MH-9	Qvof1	Gneiss	33.6578	115.9804	545	60/35/20	5	15.056	1.0062
MH-10	Qvof1	Gneiss	33.6580	115.9821	545	60/50/20	5	15.190	0.9967
MH-11	Qvof1	Granite	33.6580	115.9804	560	70/85/17	5	15.076	1.0023
MH-13	Qvof2	Granite	33.6778	115.9907	528	55/25/20	5	15.662	1.0109
MH-14	Qvof2	Granite	33.6746	115.9899	525	40/130/35	5	14.882	0.9981
MH-15	Qvof2	Quartzite	33.6742	115.9906	517	40/30/50	5	15.933	0.9645
MH-17	Qyf1	Granite	33.6093	116.0286	81	80/60/35	5	15.454	0.9849
MH-18	Qyf1	Gneiss	33.6092	116.0287	77	75/60/25	5	15.110	0.9964
MH-19	Qyf1	Gneiss	33.6088	116.0292	90	30/60/15	5	15.941	0.9807
MH-20	Qyf1	Quartzite	33.6087	116.0294	69	75/40/40	5	15.349	0.9834
MH-21	Qyf1	Gneiss	33.6085	116.0296	86	55/25/40	5	15.281	0.9494
MH-29	Qvof2	Gneiss	33.5807	115.9920	97	55/80/30	5	15.369	0.9918
MH-30	Qvof2	Quartzite	33.5798	115.9925	87	90/70/40	5	15.120	1.0058
MH-32	Qvof2	Gneiss	33.5798	115.9925	87	60/80/35	5	15.192	1.0202
MH-41	Qvof2	Quartzite	33.5324	115.9098	56	40/50/20	5	15.103	0.9979
MH-42	Qvof2	Gneiss	33.5324	115.9098	56	25/45/20	5	15.058	0.9907
MH-43	Qvof2	Quartzite	33.6800	116.0975	123	70/150/30	5	23.010	0.9822
MH-44	Qvof2	Granite	33.6805	116.0963	134	75/100/20	5	23.306	1.0149
MH-46	Qvof2	Quartzite	33.6820	116.0931	154	30/45/20	5	24.256	0.9525
MH-47	Qvof2	Granite	33.6856	116.0978	143	40/45/20	5	15.096	0.9827
MH-49	Qvof2	Quartzite	33.6690	116.0902	98	25/25/10	5	27.022	0.9797
MH-50	Qvof2	Quartzite	33.6690	116.0902	103	35/15/5	5	26.293	1.0034
MH-51	Qvof2	Granite	33.6689	116.0905	99	35/15/12	5	22.734	0.9632
MH-HG-4	Jos	Granite	33.6166	115.9176	278	40/60/40	5	15.487	0.3481
MH-HG-5	Jos	Gneiss	33.6168	115.9175	275	160/150/100	5	5.4317	0.3521
MH-HG-8	Qac	Granite	33.5829	115.9813	57	80/90/40	5	19.933	0.3483
MH-HG-9	Qac	Granite	33.5836	115.9811	57	70/80/50	5	11.264	0.3461
MH-HG-10	Qac	Gneiss	33.5832	115.9823	56	120/105/75	5	24.606	0.3479
MH-HG-11	Qvof2	Granite	33.6861	116.0970	146	40/30/20	5	20.499	0.3478
MH-HG-12	Qvof2	Granite	33.6861	116.0962	150	50/20/20	5	11.883	0.351
MH-HG-13	Qvof2	Granite	33.6863	116.0950	146	90/70/20	5	12.111	0.3483
MH-HG-35	Qvof2	Gneiss	33.5338	115.9062	43	50/30/20	5	29.099	0.3481
MH-HG-2-1	Qt1	Gneiss	33.5987	115.9689	157	30/40/40	5	29.215	0.3535
MH-HG-2-3	Qt1	Granite	33.5990	115.9687	157	70/50/30	5	16.425	0.3629
MH-HG-2-4	Qt1	Gneiss	33.5985	115.9690	156	90/50/45	5	29.833	0.3548
MH-HG-2-5	Qvof1	Gneiss	33.5980	115.9420	270	65/60/25	5	25.067	0.3606
MH-HG-2-6	Qvof1	Gneiss	33.5963	115.9422	262	65/55/30	5	14.908	0.6527
MH-HG-2-7	Qvof1	Granite	33.5981	115.9421	270	85/50/30	5	29.033	0.3414

[a] Corrected for blanks run concurrent with sample measurement.
[b] Samples MH-7 through MH-51 measured at Lawrence Livermore National Laboratory, all others at PRIME lab, Purdue University.
[c] Sampled uppermost surface of boulder.
[d] Uncertainties reported to 1-σ confidence level.
[e] All ages calculated using the CRONUS online calculator version 2.2 (Balco et al., 2008; http://hess.esswashington.edu).

contains notable gneiss and schist (10–20%) among poorly sorted, subrounded sediment. Boulder splitting and pitting is very rare and no ventifacts are present. Vegetation is not diverse, exhibiting only the infrequent smoke tree, (*Dalea spinosa*) and Creosote bush (*Larrea tridentata*). The Qt1 surface can be distinguished from the Qyf1 surface only by its surface morphology where Qt1 forms terraces in river channels and Qyf1 forms alluvial fans.

4.2. Surface exposure dating

Sample locations for surface exposure ages are shown in Figs. 4 and 5; Fig. 7 displays ages as NKDE plots, and Table 7 presents the MSWD and 1-σ uncertainty of ages defined by NKDE analysis. The NKDE plots for the Qvof1 and Qvof2 surfaces exhibit a bimodal distribution whereas the plot for the Qvf1 surface resembles a positively skewed normal distribution. The ages for the Qyf1 and Qvof2 surfaces cluster best, passing the MSWD test. Sample MH-19 from the Qyf1 surface dataset and samples MH-43, -46, -49, -50, and -51 from the Qvof2 surface dataset are considered outliers according to the MSWD test results. The samples removed from each dataset during the MSWD test lie under the secondary peak seen in the NKDE plots (Fig. 7). The Qvof1 surface does not pass the MSWD test with any combination of samples from the surface. MSWD test results show an age of 8.2 ± 2.1 ka for the Qyf1 surface and an age of 67.2 ± 2.1 ka for the Qvof2 surface. The age for the Qvof1 surface is inconclusive; the primary peak in the NKDE plot is at ~217 ka and the weighted mean of boulder surface exposure ages is 266 ± 100 ka. A hypothesized extension of the Qvof1 surface in the central Mecca Hills (Fig. 5b) was sampled (samples MH-HG-2 to -5, -6, and -7); however, age results do not pass the MSWD test and are significantly younger than surface exposure ages for the Qvof1 surface farther north.

Boulders in the active channel of Box Canyon (Qac; Table 2) range in age from 6.6 ± 0.9 to 36.0 ± 3.2 ka and produce a non-MSWD weighted mean age of 8.4 ± 16 ka. Samples from the first river terrace level present in the central Mecca Hills (Qt1) produce a weighted mean age of 9.0 ± 4.8 ka that does not pass the MSWD test. Two boulders present on a strath terrace at the uppermost reaches of Box Canyon produced surface exposure ages of 39.3 ± 3.4 ka and 13.3 ± 1.8 ka.

Depth profile data for surfaces Qyf1, Qvof2, and Qvof1 produce ages of 2.60 + 6.85/−0.10 ka, 17.4 + 14.8/−3.5 ka, and 280 + 164/

Be Carrier Concentration (mg/g)	Be^{10} / Be^{9} ratio[2] (blank corrected) (10^{-14})	Be^{10} (atoms)[a] (10^{-14})	AMS Standard[b]	Time-Independent[d] Lal 1991 /Stone 2000 (ka)	Desilets et al.[d] 2003/06 (ka)	Dunai[d] 2001 (ka)	Lifton et al.[d] 2005 (ka)	Time-dependent[d] Lal 1991/Stone 2000 (ka)
0.44	142.20 ± 3.34	277 ± 6.52	LLNL3000	468.8 ± 47.5	483.7 ± 65.8	463.9 ± 62.5	464.8 ± 53.0	431.5 ± 42.1
0.44	120.10 ± 2.85	236 ± 5.61	LLNL3000	390.3 ± 38.8	397.6 ± 52.9	383.4 ± 50.6	383.6 ± 42.9	356.2 ± 34.1
0.44	84.57 ± 2.31	163 ± 4.46	LLNL3000	261.5 ± 25.4	264.5 ± 34.2	255.4 ± 32.8	255.1 ± 27.8	238.8 ± 22.5
0.44	78.05 ± 1.90	153 ± 3.72	LLNL3000	240.5 ± 23.1	242.5 ± 31.0	234.0 ± 29.8	233.4 ± 25.1	218.8 ± 20.3
0.404	22.11 ± 0.70	38.6 ± 1.22	KNSTD3110	59.5 ± 5.6	61.7 ± 7.7	59.8 ± 7.4	59.8 ± 6.3	55.5 ± 5.1
0.404	56.13 ± 1.58	102 ± 2.86	KNSTD3110	161.3 ± 15.3	163.4 ± 20.6	157.8 ± 19.8	157.5 ± 16.8	147.7 ± 13.6
0.404	12.74 ± 0.58	20.8 ± 0.95	KNSTD3110	32.2 ± 3.2	34.1 ± 4.4	33.0 ± 4.2	33.2 ± 3.6	30.8 ± 3.0
0.44	1.91 ± 0.51	3.58 ± 0.96	LLNL3000	7.8 ± 2.2	8.8 ± 2.6	8.6 ± 2.5	8.7 ± 2.5	7.7 ± 2.2
0.44	2.59 ± 0.51	5.03 ± 0.99	LLNL3000	11.0 ± 2.4	12.6 ± 2.9	12.2 ± 2.8	12.4 ± 2.7	11.0 ± 2.3
0.44	3.75 ± 0.52	6.79 ± 0.94	LLNL3000	14.6 ± 2.4	16.6 ± 3.0	16.1 ± 2.9	16.3 ± 2.8	14.6 ± 2.4
0.44	1.45 ± 0.50	2.74 ± 0.94	LLNL3000	6.0 ± 2.2	6.8 ± 2.5	6.7 ± 2.5	6.8 ± 2.5	6.0 ± 2.2
0.44	2.15 ± 0.47	3.93 ± 0.86	KNSTD3110	8.5 ± 2.0	9.7 ± 2.4	9.4 ± 2.3	9.6 ± 2.3	8.5 ± 2.0
0.44	16.96 ± 0.73	32.2 ± 1.39	LLNL3000	70.0 ± 6.9	74.2 ± 9.5	71.7 ± 9.1	72.1 ± 7.9	66.8 ± 6.4
0.44	16.51 ± 0.66	32.3 ± 1.29	LLNL3000	70.9 ± 6.9	75.1 ± 9.5	72.5 ± 9.2	73.0 ± 7.9	67.6 ± 6.4
0.44	18.07 ± 0.70	35.7 ± 1.38	LLNL3000	78.5 ± 7.6	83.2 ± 10.5	80.3 ± 10.1	80.9 ± 8.7	74.7 ± 7.1
0.44	16.44 ± 0.66	32.0 ± 1.28	LLNL3000	72.0 ± 7.0	76.3 ± 9.7	73.7 ± 9.3	74.2 ± 8.1	68.7 ± 6.5
0.44	17.89 ± 0.69	34.7 ± 1.34	LLNL3000	78.1 ± 7.6	82.9 ± 10.5	80.0 ± 10.1	80.6 ± 8.7	74.6 ± 7.0
0.404	46.17 ± 1.56	53.3 ± 1.80	LLNL3000	114.5 ± 11.0	118.4 ± 15.0	115.0 ± 14.5	115.2 ± 12.4	107.9 ± 10.1
0.404	28.13 ± 0.86	33.1 ± 1.01	LLNL3000	69.7 ± 6.5	73.7 ± 9.1	71.3 ± 8.8	71.6 ± 7.5	66.4 ± 6.0
0.404	44.82 ± 1.33	47.6 ± 1.41	LLNL3000	99.3 ± 9.3	103.7 ± 12.9	100.6 ± 12.5	101.0 ± 10.7	94.2 ± 8.6
0.404	19.96 ± 0.93	35.1 ± 1.64	LLNL3000	73.5 ± 7.4	77.7 ± 10.0	75.1 ± 9.7	75.5 ± 8.4	69.8 ± 6.8
0.404	61.67 ± 1.55	60.4 ± 1.52	LLNL3000	133.2 ± 12.5	137.3 ± 17.1	133.2 ± 16.5	133.3 ± 14.0	124.9 ± 11.3
0.404	56.15 ± 1.82	57.9 ± 1.88	LLNL3000	126.9 ± 12.1	130.9 ± 16.5	127.0 ± 16.0	127.1 ± 13.6	119.2 ± 11.1
0.404	51.43 ± 6.97	58.9 ± 7.98	LLNL3000	129.6 ± 21.5	133.6 ± 24.8	129.6 ± 24.0	129.7 ± 22.5	121.6 ± 20.0
1.414	10.15 ± 0.18	21.6 ± 0.38	07KNSTD	41.5 ± 3.7	43.2 ± 5.2	42.0 ± 5.0	42.1 ± 4.3	39.3 ± 3.4
1.414	1.17 ± 0.11	7.18 ± 0.67	07KNSTD	13.4 ± 1.8	15.2 ± 2.4	14.7 ± 2.3	14.9 ± 2.1	13.3 ± 1.8
1.414	2.26 ± 0.03	3.74 ± 0.05	07KNSTD	8.3 ± 1.1	9.4 ± 1.5	9.2 ± 1.4	9.3 ± 1.3	8.2 ± 1.1
1.414	1.02 ± 0.07	2.97 ± 0.20	07KNSTD	6.6 ± 0.9	7.5 ± 1.2	7.3 ± 1.1	7.4 ± 1.0	6.6 ± 0.9
1.414	12.50 ± 0.33	16.7 ± 0.44	07KNSTD	37.3 ± 3.4	39.6 ± 4.8	38.4 ± 4.7	38.7 ± 4.0	36.0 ± 3.2
1.414	8.74 ± 0.33	14.0 ± 0.53	07KNSTD	28.9 ± 2.8	31.5 ± 3.9	30.5 ± 3.8	30.8 ± 3.3	28.2 ± 2.6
1.414	7.24 ± 0.16	20.2 ± 0.45	07KNSTD	41.7 ± 3.8	43.6 ± 5.3	42.5 ± 5.1	42.5 ± 4.3	39.7 ± 3.5
1.414	19.26 ± 1.20	52.4 ± 3.27	07KNSTD	110.3 ± 12.1	114.4 ± 15.7	111.1 ± 15.2	111.3 ± 13.3	104.1 ± 11.2
1.414	28.11 ± 0.74	31.8 ± 0.84	07KNSTD	72.4 ± 6.7	76.8 ± 9.5	74.2 ± 9.1	74.7 ± 7.8	69.2 ± 6.2
1.414	6.36 ± 0.90	7.28 ± 1.03	07KNSTD	14.9 ± 2.5	16.9 ± 3.1	16.3 ± 3.0	16.5 ± 2.9	14.8 ± 2.4
1.414	1.38 ± 0.16	2.88 ± 0.33	07KNSTD	5.9 ± 0.9	6.7 ± 1.1	6.6 ± 1.1	6.7 ± 1.0	6.0 ± 0.9
1.414	5.86 ± 0.19	6.59 ± 0.21	07KNSTD	13.4 ± 1.3	15.4 ± 1.9	14.8 ± 1.8	15.1 ± 1.6	13.4 ± 1.2
1.414	10.48 ± 0.44	14.3 ± 0.60	07KNSTD	26.7 ± 2.6	29.1 ± 3.7	28.1 ± 3.5	28.4 ± 3.1	26.0 ± 2.5
1.414	9.41 ± 0.14	39.0 ± 0.58	07KNSTD	74.2 ± 6.7	78.0 ± 9.5	75.4 ± 9.1	75.7 ± 7.7	70.0 ± 6.1
1.414	23.30 ± 0.80	25.9 ± 0.89	07KNSTD	48.7 ± 4.6	50.7 ± 6.3	49.0 ± 6.1	49.1 ± 5.2	45.6 ± 4.2

−117 ka respectively (Fig. 8; Tables 3 and 4). We use the Bayesian most probable age from each profile result as our preferred depth profile age based on suggestions by Hidy et al. (2010). A value of 1.00 for topographic shielding correction was used because each location had a very low horizon («20°) and a value of 1.00 for cover as no snow or vegetative cover was present or expected. We use a reference spallogenic production rate of 4.39 ± 0.19 atoms/g/a based on estimated production rates for North America (Balco et al., 2008; Lifton et al., 2009; Briner et al., 2012) and to maintain consistency with surface exposure age calculations. Following Hidy et al. (2010), we assumed 0.65–0.75 m penetration depth of neutrons, assuming an attenuation length of 160 ± 5 g/cm^2 and a material density of 2.2–2.5 g/cm3. We chose this density range due to strong presence of granite and gneiss in the sediment. We note that variations in the density through time can lead to significant uncertainty in the depth profile age (Rodés et al., 2011); we assume this value as constant without further data on the change in density with time. Additional parameters, chosen for each depth profile stimulation, are described and justified in the discussion sections.

4.3. Denudation rates

Denudation rate measurements and sampling locations are presented in Fig. 4 and Tables 5 and 6. Fig. 9 compares denudation rates with selected geomorphic parameters. We chose the geomorphic parameters of mean catchment slope, catchment area (size), mean catchment elevation, and total catchment relief, following results from Portenga and Bierman (2011), to allow to comparison with global datasets of denudation rate. Denudation rate values range from a minimum of 20 ± 3 m/Ma in the northernmost catchment to a maximum value of 89 ± 20 m/Ma at the mouth of Box Canyon. Denudation rates increase nearer to the trace of the San Andreas Fault for samples collected from the same drainage such as Box Canyon (MH-HG-3, 6, 7) and Painted Canyon (MH-HG-28, 29, 30; Fig. 4).

Denudation rates demonstrate no correlation with relief, mean elevation, or catchment size, producing R^2 values of 0.001, 0.14, and 0.031, respectively. Denudation rates correlate with mean catchment slope producing an R^2 of 0.60 using a non-linear regression (Binnie et al., 2007; Ouimet et al., 2009; DiBiase et al., 2010). A regression of denudation rate versus total mapped Quaternary fault length normalized by catchment area produced a strong correlation with an R^2 value of 0.85.

The relationship between the topography of the Mecca Hills isolated by removing the regional slopes and the denudation rate is demonstrated in Fig. 11. The greatest denudation rate occurs at Hidden Spring Canyon where topographic relief changes dramatically with distance along the San Andreas Fault. Along the profile,

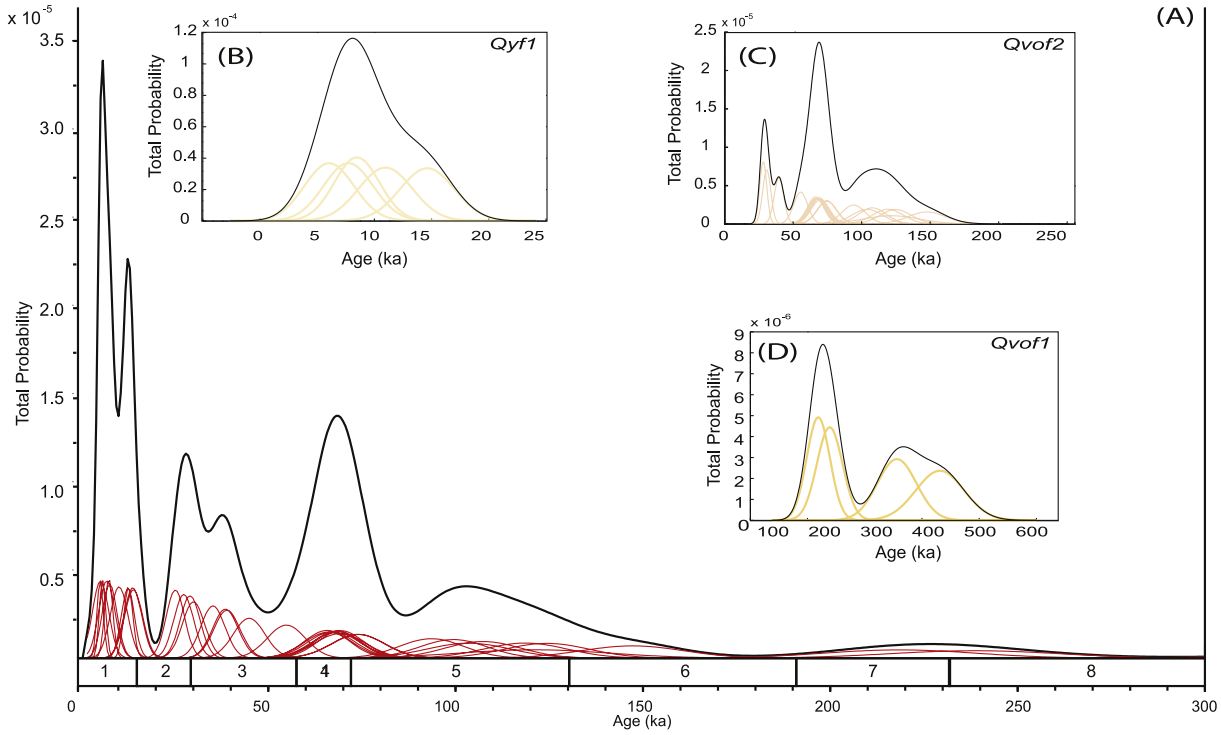

Fig. 7. (A) Normal kernal density estimate (NKDE) for ^{10}Be surface exposure ages from boulders throughout the Mecca Hills juxtaposed with marine isotope stages for the past 300 ka (Lisiecki and Raymo, 2005). Small thin curves represent individual boulder ages and error with assumed Gaussian distributions; bold black curve represents sum of individual distributions. Most probable surface ages do not seem to correlate with a consistent type of climate transition. (B) NKDE plot for boulder ages from surface Qyf1.The surface displays a most probable peak at around 7–8 ka consistent with field observations that suggest a young age. A slight positive skew is evident in the curve, which we interpret as higher ^{10}Be inheritance for sample MH-19 (Table 2). (C) NKDE plot for boulder ages from surface Qvof2. The surface illustrates a most probable peak at around 70 ka yet significant dispersion of ages is present producing an asymmetrically trimodal distribution of ages. Older ages are spatially dispersed amongst younger ages on continuous surfaces (see Fig. 5; Table 2). (D) NKDE plot for boulder ages from surface Qvof1. Surface exposure ages produce a most probable peak around 220 ka yet the surface demonstrates an asymmetrical bimodal distribution to surface Qvof2. Most probable age is consistent with results from depth profile simulation (Fig. 8).

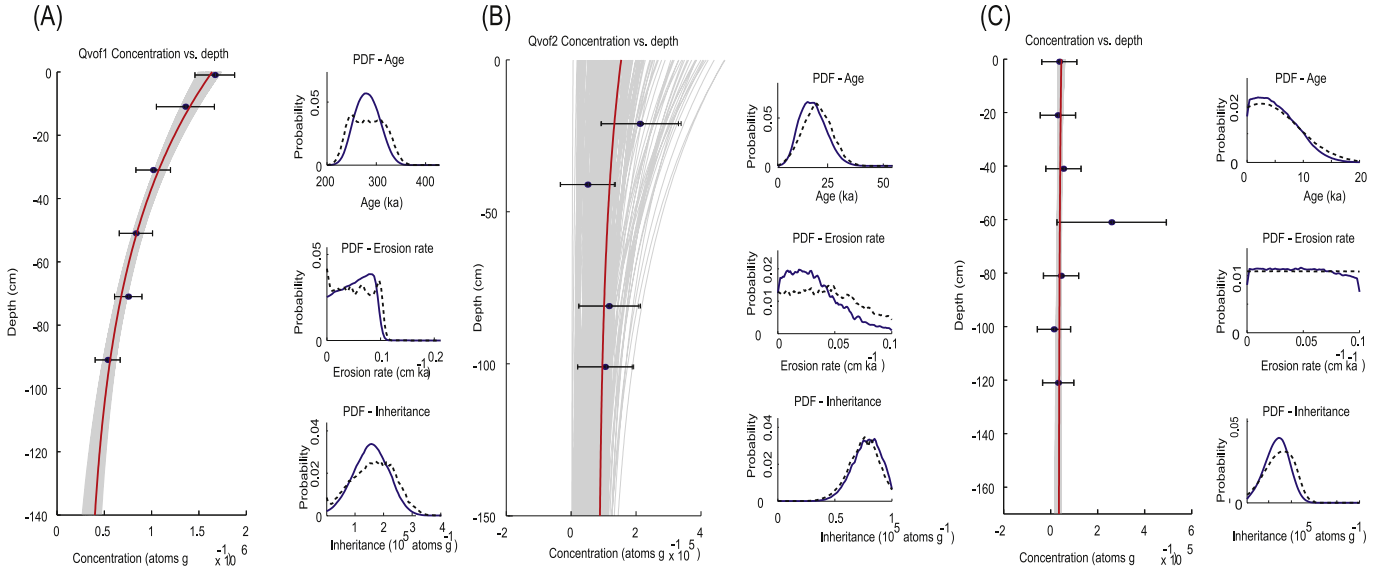

Fig. 8. Beryllium-10 depth profiles for geomorphic surfaces within the Mecca Hills. Gray curves represent profiles simulated with MATLAB code developed by Hidy et al. (2010). Subplots represent probability density functions for variables used in depth profile simulations. Red curve indicates best fit profile after more than 500000 iterations. Profile results are summarized in Table 4. Sampled locations are indicated on Fig. 5. See text for parameters used in profile simulation. (A) Depth profile of cosmogenic ^{10}Be concentrations from unit Qvof1; see Fig. 5 for location. Note the well-defined curve and approximately Gaussian distributions for age and inheritance results. (B) Depth profile of ^{10}Be concentrations from surface Qvof2 near Box Canyon; see Fig. 5 (C) Depth profile of ^{10}Be concentrations from surface Qyf1 near Painted Canyon; see Fig. 5. Note near constant concentration of ^{10}Be with depth. Profile was defined with ages obtained from surface exposure ages (Fig. 5, Table 2). (For interpretation of the references to colour in this figure legend, the reader is referred to the web version of this article.)

Table 3
^{10}Be depth profile data.

Sample name	Geomorphic Surface	Latitude °N	Longitude °W	Altitude (m)	Depth (cm)	Quartz weight (g)	^{9}Be carrier weight (g)	^{9}Be concentration (mg/g)	Standard	^{10}Be/^{9}Be corrected ratio (10^{-15})	^{10}Be (10^{-4} atoms/g SiO_2)
MH-1	Qvof1	33.657	115.981	561	0	15.2747	1.0128	0.44	LLNL3000	856 ± 15.4	167 ± 2.99
MH-2					10	15.1755	1.0218	0.44	LLNL3000	686 ± 22.1	136 ± 4.38
MH-3					30	15.2560	1.0137	0.44	LLNL3000	520 ± 13.4	102 ± 2.61
MH-4					50	15.1833	0.9972	0.44	LLNL3000	432 ± 13.0	83.4 ± 2.52
MH-5					70	15.1533	1.0060	0.44	LLNL3000	386 ± 10.6	75.3 ± 2.07
MH-6					90	15.0788	1.0006	0.44	LLNL3000	274 ± 9.7	53.6 ± 1.89
MH-22	Qyf1	33.608	116.029	70	20	15.5099	1.0787	0.44	KNSTD3110	15.0 ± 4.61	3.06 ± 0.94
MH-23					40	15.4440	1.0293	0.44	KNSTD3110	27.7 ± 4.76	5.43 ± 0.93
MH-24					60	15.2748	1.0670	0.44	KNSTD3110	126 ± 14.2	25.9 ± 2.91
MH-25					80	15.3336	1.0214	0.44	KNSTD3110	22.7 ± 4.79	4.44 ± 0.94
MH-26					100	15.1935	0.9997	0.44	KNSTD3110	7.09 ± 4.58	1.37 ± 0.89
MH-27					120	15.9202	0.9706	0.44	KNSTD3110	17.9 ± 4.64	3.22 ± 0.83
MH-28					0	15.2012	1.0452	0.44	KNSTD3110	18.2 ± 4.62	3.68 ± 0.93
MH-33	Qvof2	33.580	115.992	94	100	15.0084	1.0234	0.44	KNSTD3110	53.2 ± 4.78	21.6 ± 1.36
MH-34					80	15.1173	1.0384	0.44	KNSTD3110	58.8 ± 5.22	5.13 ± 0.94
MH-36					40	15.6107	0.9773	0.44	KNSTD3110	27.8 ± 5.13	11.9 ± 1.05
MH-37					20	16.1380	1.0215	0.44	KNSTD3110	116 ± 7.32	10.7 ± 0.96

mean elevation increases gradually from the southeastern (right) edge to a peak before decreasing downward on the northwestern (left) side of the graph. Topographic relief is greatest near the center of the range and tapers toward the edges. Uplift/fluvial incision rates on the "tectonic uplift" curve rise towards the center of the graph, peaking at Painted Canyon and tapering toward the edges of the Mecca Hills.

5. Discussion

5.1. Alluvial fan formation

The alluvial surfaces examined in this paper are regionally extensive and represent episodic deposition during the ongoing deformation and uplift of the Mecca Hills. The extent of surface Qvof1 and the present erosion of the surface by Painted Canyon and Box Canyon catchments suggests that this surface may have had a previously greater extent. Likewise, the abandonment of surface Qvof2 and further creation of Qvof2-capped terraces through river incision implies a greater continuous extent of this surface than is evident at present. The cause of the abandonment and incision of Qvof2 may also be post-depositional uplift consistent with the interpretations of other studies in the region (Sylvester and Smith, 1976). The youngest surface Qyf1 does not seem to have had a previously greater extent based on its current morphology and lack of incision.

Patt (2000) hypothesized that the depositional environment of the three major surfaces was a flash flood-controlled regime that produced extensive alluvial fans and fanglomerates, and our observations agree. The sediment composing the three surfaces is coarse and poorly sorted, requiring a high-energy environment to generate the critical shear stresses necessary to move this cobble- and boulder-size material. In the current climate of the Salton Trough, the only feasible high-energy mechanism is flash flooding in which sediment is rapidly and episodically transported from the nearby Little San Bernardino, Cottonwood, and Orocopia Mountains towards the basin floor, leaving behind extensive alluvial fans. Past climates, such as during glacial times, may have caused the region to be both colder and wetter owing to the southward migration of the mid-latitude jet stream (Owen et al., 2003) although this mechanism is under considerable debate (Miller et al., 2010; Antinao and McDonald, 2013). This may have shifted the dominant sediment transport process towards river flow and aggradation (Bull, 1991; Miller et al., 2010). We interpret the ages of the surfaces derived from ^{10}Be surface exposure dating to reflect abandonment ages when a change in the relationship between sediment supply and fluvial transport capacity, such as during climate change (Fig. 7), caused drainage systems to shift from aggradation to incision (Burbank and Anderson, 2011).

5.2. Surface exposure and depth profiles ages

5.2.1. Active channel deposits (Qac), river terrace deposits (Qt1) and boulder inheritance

Surface exposure dating in arid environments requires an analysis of the potential for inherited ^{10}Be obtained prior to deposition of alluvial units and surfaces. Beryllium-10 ages derived from boulders in the active channel deposits, Qac, illustrate the complex nature of ^{10}Be inheritance in the Mecca Hills (Table 2). The large range of ages from 6.6 ± 0.9 to 36.0 ± 3.2 ka may suggest that individual boulders undergo a complex exposure and transport history. Granitic and gneissic boulders in active channels can have two primary sources: the Little San Bernardino and Orocopia Mountains to the north and east where bedrock is exposed; and from within the strata of the Mecca Hills, where boulders can be seen eroding out of coarse grained units. These two sources should have varying exposure histories and therefore varying levels of ^{10}Be concentration, the former generating inheritance during exposure on hillslopes and during sediment transport prior to deposition. In the case of the latter, sediment after traveling and obtaining ^{10}Be will be buried and presumably enter a net loss of ^{10}Be as radioactive decay supersedes nuclide production. Because the strata of the Mecca Hills is in some places younger (Rymer, 1991) than the half-life of ^{10}Be (1.39 Ma; Balco and Shuster, 2009), a boulder buried and exhumed from within the Mecca Hills may still retain significant ^{10}Be from its prior exposure, transport, and deposition. Furthermore, it may be expected that sediment that is younger than 3–4 ^{10}Be half-lives will contain significant inheritance. An example of the complications of inheritance issues can be found in the surface exposure ages for a sample fill terrace within the Mecca Hills (Qt1; Table 2; Fig. 5). The ages for the surface suggest an age near the MIS 1/2 transition (14.8 ± 2.4, 6.0 ± 0.9, and 13.4 ± 1.2 ka); however, all

Table 4
^{10}Be depth profile simulation results.

Surface name	Age[a] (ka)	Inheritance[b] (104 atoms/g SiO_2)	Surface Lowering[c] (cm ka^{-1})
Qvof1			
Mean	280.3	15.70	0.05
Median	279.2	15.70	0.05
Mode	280.1	15.99	0.08
Min chi^2	266.6	27.92	0.05
Maximum	369.5	38.60	0.12
Minimum	202.6	0.10	0.00
Bayesian most probable	279.9	16.24	0.08
Bayesian 2-σ upper	328.3	27.00	0.10
Bayesian 2-σ lower	234.7	3.14	NaN
Qvof2			
Mean	28.8	5.00	0.03
Median	19.2	5.01	0.02
Mode	5.6	6.94	0.01
Min chi^2	17.2	8.15	0.04
Maximum	100.0	10.00	0.10
Minimum	0.0	0.00	0.00
Bayesian most probable	17.4	8.48	0.01
Bayesian 2-σ upper	29.6	9.72	0.09
Bayesian 2-σ lower	5.5	5.02	0.00
Qyf1			
Mean	4.4	2.92	0.05
Median	4.3	2.89	0.05
Mode	2.0	2.84	0.07
Min chi^2	2.7	3.27	0.05
Maximum	10.8	4.73	0.10
Minimum	0.0	1.14	0.00
Bayesian most probable	2.6	3.01	0.04
Bayesian 2-σ upper	13.7	4.63	0.10
Bayesian 2-σ lower	0.1	0.55	0.00

[a] 10Be data for depth profile simulation included in Supplemental Table 2; all samples run at Lawrence Livermore National Laboratory.
[b] Parameters for each depth profile simulation described and justified in text.
[c] Although surface lowering is reported, these values subject to an assumed constraint of near zero (see methods) and cannot be used to describe erosion rate.

are less than the age of sample MH-HG-10 (36.0 ± 3.2 ka) taken from the active channel downstream. Whether the true age is expressed in the sampled terrace boulders or if these are values dominated by inheritance is not clear. The varying nature of the inheritance warrants caution in interpreting boulder surface exposure ages and the determination of the true age of the alluvial fan surfaces (Blisniuk et al., 2012). We note that the boulder surface ages act as age maxima for the surfaces.

5.2.2. Age and evolution of Qyf1

The Qyf1 surface shows the tightest distribution of surface exposure ages ranging from 6.0 ± 2.2 ka to 14.6 ± 2.4 ka (Table 2; Fig. 7). The NKDE plot for the Qyf1 surface has one distinct peak at ~8 ka with a slight positive skew to the distribution (Fig. 7). Surface Qyf1 passes the MSWD test with the removal of sample MH-19 and produces a weighted mean surface exposure age of 8.2 ± 2.1 ka. This age is significantly younger than the ages of Qvof1 and Qvof2 consistent with geomorphic field observations suggesting this is a young surface: Qyf1 lacks of rock varnish and has no development of desert pavement. Depth profile simulations were defined using the same parameters used for the older surfaces and subject to a constraint of assumed minimal erosion while the program optimized the age and inheritance. The simulation produced a Bayesian most probable age of 2.6 +5.6/−1.3 ka and an inheritance value of 3.0 +0.8/−1.0 × 10^4 atoms/g SiO_2. The modeled inheritance values correspond to an inherited age of 6.5 ± 1.9 ka calculated from the CRONUS calculator (Balco et al., 2008). This indicates that ^{10}Be inheritance dominates the signal from the depth profile. The single peak in the NKDE plot for the Qyf1 surface illustrates the greater

Table 5
Denudation rate calculation results.

Sample name	Drainage system	Latitude °N	Longitude °W	Attenuation length (m)	Quartz mass (g)	^{9}Be carrier (g)	Be carrier concentration (mg/g)	^{10}Be/ ^{9}Be ratio[a] (blank corrected) (10^{-15})	AMS standard[b]	^{10}Be atoms[c] (10^{-4})	Basin wide erosion rate[d] (m / Ma)	Applicable age range (ka)
MH-HG-3	Box Canyon	33.6249	115.9079	0.6	26.0483	0.3495	1.4140	128 ± 3.10	07KNSTD	16.2 ± 0.39	26.6 ± 3.75	23
MH-HG-6	Box Canyon	33.5894	115.9274	0.6	34.1162	0.3501	1.4140	151 ± 5.10	07KNSTD	14.7 ± 0.49	28.7 ± 3.81	21
MH-HG-7	Box Canyon	33.5830	115.9821	0.6	31.0901	0.3486	1.4140	45.1 ± 8.10	07KNSTD	4.78 ± 0.86	89.2 ± 19.6	7
MH-HG-15	Thermal Canyon	33.6627	116.0843	0.6	31.8451	0.3493	1.4140	90.1 ± 5.10	07KNSTD	9.34 ± 0.53	39.8 ± 5.61	15
MH-HG-24	NW Mecca Hills	33.6824	116.0985	0.6	18.9745	0.3538	1.4140	82.1 ± 8.10	07KNSTD	14.5 ± 1.43	19.9 ± 3.17	30
MH-HG-29	Painted Canyon	33.6300	115.9901	0.6	33.0013	0.3524	1.4140	57.1 ± 3.10	07KNSTD	5.76 ± 0.31	36.5 ± 19.3	16
MH-HG-30	Painted Canyon	33.6165	115.9988	0.6	33.6224	0.3489	1.4140	43.1 ± 6.10	07KNSTD	4.23 ± 0.60	53.1 ± 7.84	11
MH-HG-28	Painted Canyon	33.6066	116.0229	0.6	34.0055	0.3476	1.4140	95.3 ± 48.9	07KNSTD	9.20 ± 4.72	75.3 ± 14.6	8
MH-HG-34	SE Drainage	33.5332	115.9104	0.6	31.4809	0.3489	1.4140	39.3 ± 2.90	07KNSTD	4.12 ± 0.30	75.8 ± 11.6	8
MH-HG-ER2	Thermal Canyon	33.6644	116.0548	0.6	18.4268	0.3588	1.4140	38.6 ± 0.39	07KNSTD	71.1 ± 0.72	53.2 ± 6.78	11
MH-HG-ER3	Hidden Spring	33.5582	115.9416	0.6	22.9891	0.3490	1.4140	13.1 ± 1.04	07KNSTD	18.8 ± 1.50	150 ± 22.5	4

[a] ^{10}Be production rates and topographic shielding calculated using MATLAB v. (2009) following the methods of Dortch et al., 2011.
[b] Applicable age range following Lal (1991).
[c] ^{10}Be measurements made at PRIME lab, Purdue University. See Supplemental data Table 2 for standards used and AMS results.
[d] Catchment parameters determined using ArcGIS 10.1 Student Version and USGS NED DEMs.

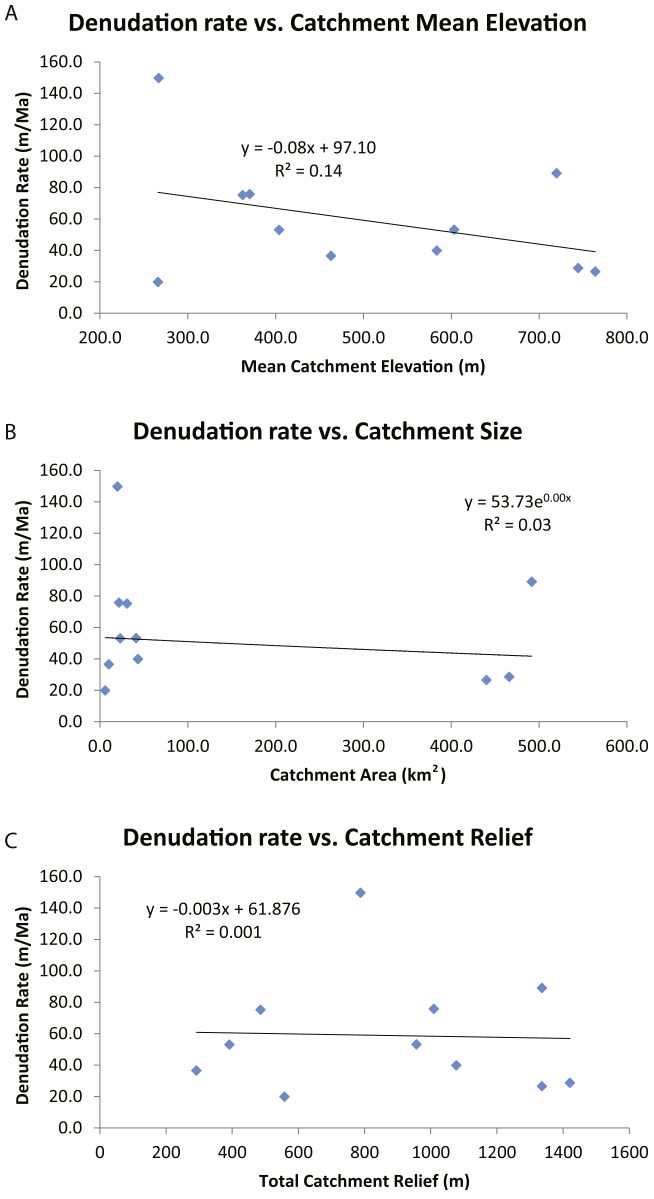

Fig. 9. ^{10}Be catchment wide denudation rates from catchments within the Mecca Hills compared to various geomorphic metrics. (A) Mean catchment elevation produced no apparent correlation with denudation rate. (B) No apparent relationship exists between catchment size and denudation rate. (C) Catchment relief, taken as the difference of maximum and minimum elevation within the catchment, also has no correlation with denudation rate.

consistency of the individual ages composing the boulder surface exposure age compared to the Qvof1 and Qvof2 surfaces. The MSWD test is easily satisfied with the removal of sample MH-19, which we interpret as containing higher ^{10}Be inheritance than the other sampled boulders.

For younger geomorphic surfaces, ^{10}Be inheritance is of greater importance in age considerations (Owen et al., 2011). The inheritance and age determination produced by the depth profile simulation, however, demonstrate that the boulder surface exposure ages are indistinguishable within 1-σ uncertainty from those produced entirely from inheritance (Tables 2 and 4). Unlike the Qvof1 and Qvof2 surfaces, the Qyf1 surface is located on an alluvial fan whose feeder catchment is composed completely of the Palm Spring and Mecca Formations. The feeder catchment therefore does not deliver boulders derived directly from crystalline bedrock such as gneiss/granitic boulders from the Little San Bernardino Mountains or greenschist from the Orocopia Mountains (Dibblee, 1954; Sylvester and Smith, 1976; Boley et al., 1994). Boulders are present at various levels in these two formations so the exact source(s) within the catchment cannot be determined. The burial time of the boulders within the formations may have been long enough to allow all inherited ^{10}Be to decay. These "reset" boulders are then brought to the surface and transported to the alluvial fan essentially simultaneously, each gaining a similar amount of ^{10}Be inheritance. When the modeled inherited ^{10}Be values are subtracted from the mean ^{10}Be value of surface boulders, the weighted mean surface exposure age is 2.4 ± 3.1 ka consistent with depth profile model findings if it is assumed that the inheritance in sand is equivalent to that in boulders. We conclude that the most likely age for the Qyf1 surface is 2.6 +5.6/−1.3 ka based on the age produced from the depth profile and consider the surface boulder ages as containing significant inheritance enough to skew the true age.

5.2.3. Age and evolution of Qvof2

The range of ^{10}Be boulder exposure ages obtained for the Qvof2 surface is large, from 66.4 ± 6.0 to 124.9 ± 11.3 ka (Table 2). The NKDE plot for the Qvof2 surface displays a bimodal curve with the primary peak at ~70 ka and the secondary peak at ~118 ka. The Qvof2 surface ages passes the MSWD test and produces a weighted mean of 69.5 ± 3.5 ka only after the removal of samples MH-43, -46, -49, -50, and -51, which were identified as outliers. The samples removed from the first MSWD test pass a second MSWD test with the removal of sample MH-46, producing a weighted mean age of ~105 ± 11 ka. The remaining surface samples form a third group that passes the MSWD test with an age of 29.5 ± 1.3 ka; however, these samples are spatially distant from each other. Depth profile results from the Qvof2 surface near Box Canyon produce a significantly younger Bayesian most probable age of 17.4 ± 6.1 ka and an inheritance value of 8.5 ± 0.6 × 10^4 atoms/g SiO_2 assuming minimal surface lowering. The depth profile simulation of Qvof2 used the same parameters as for Qvof1 and constrained the surface lowering rate to between 0.0 and 1.0 m/Ma and allowing the program to optimize surface exposure age and inheritance. The modeled inheritance value approximates an inherited age of 18 ± 2 ka based on the time-dependent exposure age model (Lal, 1991; Stone, 2000; Balco et al., 2008). The low number of samples may hinder our depth profile model as only four out of five samples were successfully measured via AMS.

Associating geologic events with the bimodal age peaks suggests that the alluvial surface mapped as Qvof2 formed over multiple episodes during climate fluctuations in MIS 5 (Fig. 7). The eventual abandonment of the surface must have occurred after the last episode of boulder deposition at 67.2 ± 5.3 ka. Because this surface did not form as the result of one event, our sampling is biased toward younger ages because we avoided weathered boulders. The depth profile simulation results contradict the surface exposure age data significantly and indicate that an underlying assumption, namely zero inheritance, may be incorrect. Whereas the surface exposure ages derived from boulders immediately above the depth profile sampling location indicate an age of ~60–70 ka, this contrasts with the depth profile-derived surface exposure age of 17.4 ± 6.1 ka. Two possible scenarios may have created this disparity: (1) our assumption of minimal surface erosion is incorrect and the depth profile underestimates the true surface age; or (2) boulders on the Qvof2 surface near Box Canyon contain significant ^{10}Be inheritance creating apparently older surface exposure ages. The Qvof2 surface near Box Canyon displays significant rock varnish on boulders and weak desert pavement formation. Significantly more relief is present on the Qvof2 surface than on the older surface (Qvof1) where our minimal erosion rate

Table 6
Denudation Rate and geomorphic variables for catchments.

Name	Drainage system	Latitude °N	Longitude °W	^{10}Be concentration (10^3 atoms/g SiO_2)	Attenuation length (m)	Basin wide erosion rate (m/Ma)	Applicable age range (ka)	Mean basin slope (°)	Basin relief (m)	Basin size (km^2)	Mean basin elevation (m asl)	Quaternary fault length (m)	Fault length normalized by catchment area (m/km^2)
MH-HG-3	Box Canyon	33.6249	115.9079	162.4 ± 3.9	0.6	26.6 ± 3.8	22.6	10.9	1336	440.0	764	9024	21
MH-HG-6	Box Canyon	33.5894	115.9274	146.5 ± 4.9	0.6	28.7 ± 3.8	20.9	11.2	1420	466.0	744	11478	25
MH-HG-7	Box Canyon	33.5830	115.9821	47.8 ± 8.6	0.6	89.2 ± 19.6	6.7	11.6	1336	491.7	720	31688	64
MH-HG-15	Thermal Canyon	33.66268	116.0843	93.4 ± 5.3	0.6	39.8 ± 5.6	15.1	10.9	1077	43.4	583	7107	164
MH-HG-24	NW Mecca Hills	33.6824	116.0985	144.6 ± 14.3	0.6	19.9 ± 3.2	30.1	7.3	558	6.0	266	485	80
MH-HG-28	Painted Canyon	33.6300	115.9901	92.0 ± 47.2	0.6	36.5 ± 19.3	16.4	12.7	292	10.0	463	1875	187
MH-HG-29	Painted Canyon	33.6165	115.9988	57.6 ± 3.1	0.6	53.1 ± 7.8	11.3	15.1	391	23.0	404	6436	279
MH-HG-30	Painted Canyon	33.6066	116.0229	42.3 ± 6.0	0.6	75.3 ± 14.6	8.0	17.4	486	30.8	362	12123	393
MH-HG-34	SE Drainage	33.5332	115.9104	41.2 ± 3.0	0.6	75.8 ± 11.6	7.9	16.6	1009	21.8	370	8101	371
MH-HG-ER2	Thermal Canyon	33.6644	116.0548	71.1 ± 0.7	0.6	53.2 ± 6.8	11.3	11.0	957	41.3	603	1486	36
MH-HG-ER3	Hidden Spring	33.5582	115.9416	18.8 ± 1.5	0.6	149.7 ± 22.5	4.0	16.8	788	20.0	267	13641	683

assumption is stronger, suggesting that erosion on the surface may have played a large role in our surface age calculation.

Another possibility to explain the variation in ages calculated from Qvof2 is that the mapped Qvof2 surface near Box Canyon does not correlate with the mapped Qvof2 surface in the northwestern Mecca Hills and is instead an uplifted section of the underlying Ocotillo Formation. If so, the depth profile results would express a young surface exposure age and the surface boulders, having persisted since initial deposition as the now eroded Qvof2, would preserve a greater apparent surface exposure age. The contact between the Ocotillo Conglomerate and the Qvof2 surface is not distinct as both alluvial fans are composed of the same lithologies and no clear horizon between units is apparent. We conclude that the surface of Qvof2 most likely has an age of 67.2 ± 5.3 ka as indicated by the boulder surface exposure ages and that the apparently young age produced from the depth profile simulation is an artifact created from a highly eroded surface.

5.2.4. Age and evolution of Qvof1

The two strong peaks in the NKDE plot for the Qvof1 surface preclude us from obtaining a single surface abandonment age. The bimodal distribution in the exposure age data suggests that post-depositional processes may have complicated the interpretation of ^{10}Be concentrations. These processes include *in situ* boulder erosion (Putkonen and Swanson, 2003) and the possibility of recycled alluvial fan material introducing boulders with significant ^{10}Be inheritance (Anderson et al., 1996). Very dark rock varnish and desert pavements are present on the Qvof1 surface (Fig. 6), which suggests long-term stability and could be taken to support an assumption of zero surface erosion and long-term surface stability (Matmon et al., 2009). The presence of desert pavements and rock varnish, however, does not ensure stability of individual boulders on the surface as fan formation can occur on timescales shorter than 50 ka, during which boulders can be eroded and rock varnish can develop on fresh surfaces (McFadden et al., 1989; Amit et al., 1993). Processes such as salt shattering of gravel and larger clasts (Amit et al., 1993) or abrasive aeolian erosional processes (Lancaster, 1984) can act to reduce ^{10}Be concentration from boulder surfaces (Behr et al., 2010). The weighted mean age for the Qvof1 surface is ~266 ± 100 ka, so boulder erosion over this timescale is likely. With the exception of inheritance, erosive processes act to reduce ^{10}Be concentration; so the age derived from the Qvof1 surface is best regarded as a minimum. We cannot rule out the possibility of inheritance of ^{10}Be as a source of scatter because the mechanism of sediment and boulder transport via flash flooding processes could deposit older material onto surfaces. Beryllium-10 inheritance is commonplace on alluvial fan surfaces (Anderson et al., 1966; Gosse and Phillips, 2001; Owen et al., 2011). Field observations within the Mecca Hills indicate that boulders are present in river sediments and suggest that there is significant possibility for inherited and pre-depositional creation of ^{10}Be during transport and final deposition.

The ^{10}Be depth profile for the Qvof1 surface provides a Bayesian most probable age of 280 ± 24.2 ka, 16.24 ± 5.38 × 10^4 atoms/g SiO_2 for inheritance, and a surface erosion rate of 0.5 ± 0.1 m/Ma (Table 4). We assumed minimal surface erosion and chose to constrain the simulation erosion rate value between 0.0 and 1.0 m/Ma. Age and inheritance was left unconstrained and the most probable best fit was determined by the profile simulator. The Bayesian most probable result for inheritance corresponds to an age inheritance of 37 ± 31 ka based on the local production rate. The weighted mean surface exposure age for surface Qvof1 is in agreement with the depth profile results. Adding the inheritance years to the surface age uncertainty may help explain the large scatter in the ages obtained from surface boulders. If the age of the

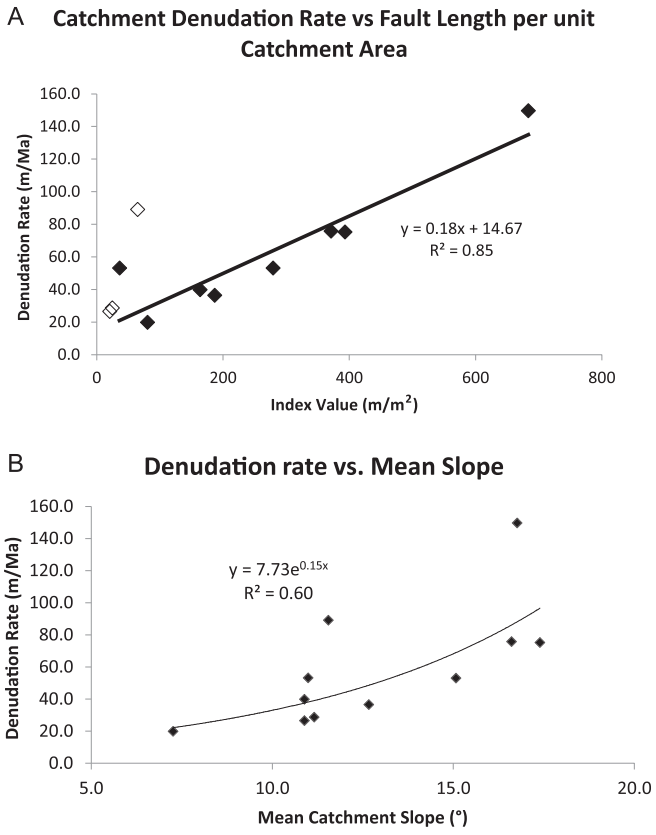

Fig. 10. Comparison of (A) catchment area normalized by total mapped faults length and (B) slope with denudation rate. White diamonds in A are measurements made in the Box Canyon catchment and are excluded from the regression as the vast majority of the catchment lies outside of the Mecca Hills.

Qvof1 surface is ~280 ± 24 ka, then the strong outlier MH-7 at 431 ± 42 ka (Table 2) may be indicative of recycling of older alluvial fan boulders with significant ^{10}Be inheritance. We acknowledge that the ^{10}Be inheritance from boulders will be different from pebble and sand sized grains due to differences in erosion and transport processes (i.e., boulders moving via high energy flows versus low energy for sand) and the strong divergence in age between boulders and depth profiles. Samples MH-10 and MH-11 mark the lower bound of the age scatter and likely deviate from the depth profile results due to boulder erosion and removal of ^{10}Be. However, there is scatter in the boulder ages and profile-based ages cannot unequivocally distinguish erosion processes from exposure processes. The agreement between the profile-based and boulder-based exposure ages does give us some confidence that the age of this surface is ~280 ka.

5.2.5. Climate influence

Previous work on the formation and abandonment of alluvial fan surfaces has generally focused on climate-based mechanisms for aggradation and incision (Bull, 1991; Ritter et al., 1995; Spelz et al., 2008). One generally accepted model for alluvial fan aggradation in the southwestern USA coincides with an increase in aridity during glacial to interglacial climate transitions (Bull, 1991, 2000; Wells et al., 1987, 1990). It has also been proposed that alluvial fan formation occurs during periods of increased precipitation (Harvey et al., 1999a, 1999b). Work by Miller et al. (2010) demonstrated that alluvial fan formation may be asynchronous with the arid model for the American Southwest and that alluvial fan formation correlates instead with increased sea surface temperatures and increased storm activity, which is known to be a significant driver of alluvial fan aggradation (Wells and Harvey, 1987). However, near the San Gorgonio Pass area of the San Bernardino Mountains, ~50 km NW of our study area, Owen et al. (2014) showed that alluvial fan formation reflects a complex mixture of allocyclic factors, such as those described above, and autocyclic factors.

Correlating episodes of alluvial fan formation in the Mecca Hills with climatic events is challenging owing to the large uncertainty associated with the dating methods. The Qyf1, Qvof1, and Qvof2 surfaces date to MIS 1, 4, and 7, respectively. However, this correlation is uncertain owing to the large scatter of ages on individual surfaces. The Qyf1 surface is contemporaneous with multiple episodes of alluvial fan aggradation during the Holocene (Miller et al., 2010) when age results from depth profile simulation are considered. The age for the Qvof1 surface derived from surface boulders (266 ± 100 ka) is too imprecise to ascertain a climate correlation nor does the depth profile age 280 ± 24 ka elucidate a possible triggering event. Surface Qvof2 matches a period of alluvial fan formation observed throughout the southwestern USA around 60–70 ka (Owen et al., 2014). While acknowledging that alluvial fan formation is likely a function of climate-modulated sediment supply (Ritter et al., 1995), the current Mecca Hills age data cannot be correlated with specific climate events.

5.2.6. Regional correlation

Owen et al. (2014) compiled 362 ^{10}Be surface exposure ages from boulders from various studies in southwestern North America to determine whether distinct depositional episodes could be identified. Owen et al.'s study demonstrates probability peaks in the ^{10}Be data at approximately 7–8 ka, 17–19 ka, 45–47 ka, 64–66 ka, and a broad peak at 160–170 ka. The addition of the data from this study does not shift the regional probability peaks significantly. The compilation in Owen et al. (2014) does not attempt to compensate for sampling biases such as studies collecting numerous samples on specific fan surfaces (Van der Woerd et al., 2006; Behr et al., 2010; Owen et al., 2014) or geologic biases due to declining boulder preservation with time.

The Qyf1, Qvof1, and Qvof2 surfaces loosely correlate with regional episodes of fan deposition. The Qyf1 surface age of the depth profile simulation, 2.6 +5.6/−1.3 ka, is significantly younger than any regional depositional episode described by Owen et al. (2014). The Qvof2 surface age is in good agreement with the regional depositional episode at 64–66 ka (Owen et al., 2014). Older ages from the Qvof2 surface that produce an MSWD test-passing weighted mean age of 117 ± 7 ka do not correlate with a regional episode of deposition (Owen et al., 2014). Qvof2 may record a local period of alluvial fan formation out of synchronicity with the regional depositional episode, assuming that inheritance is minimal. If inheritance is not minimal, older boulders on Qvof2 may be recycled older fan material, possibly from Qvof1. The Qvof1 surface appears to be significantly older than any regional depositional episode (Owen et al., 2014). The surface exposure age from boulders on the Qvof1 surface may be the oldest surface exposure age currently obtained in the region.

5.3. Denudation rates

Calculating denudation rates from ^{10}Be concentrations in active sediment assumes that the sample is representative of the denudation of entire catchment (Bierman and Steig, 1996; Granger et al., 1996). In the Mecca Hills, episodic flood events are the primary drivers of sediment transport which brings into question the assumption of representative mixing and denudation. In interpreting our denudation rates, we assume that random flash

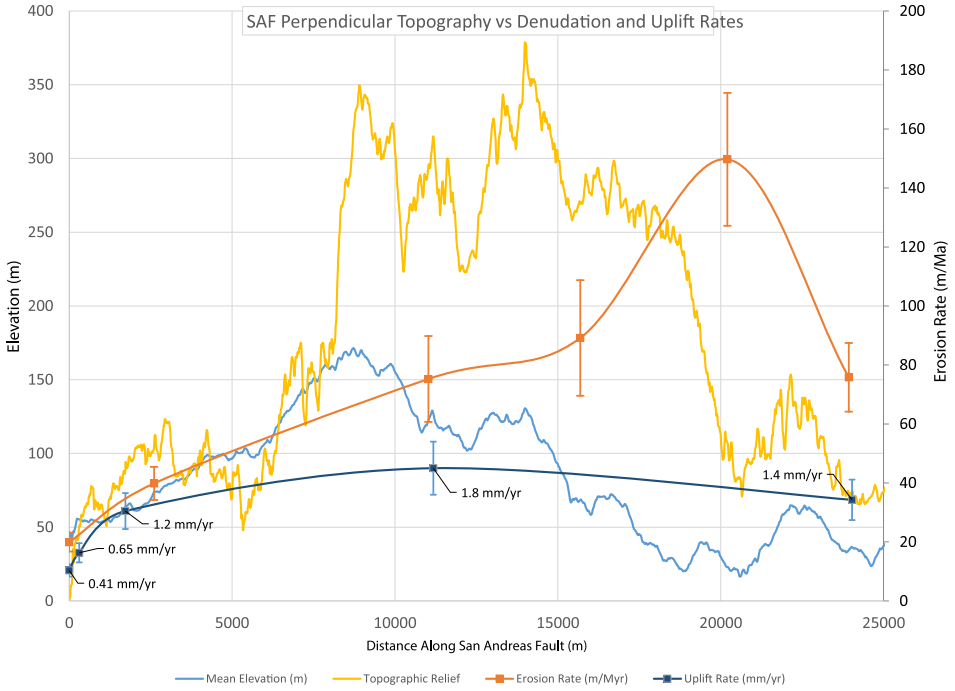

Fig. 11. Comparison of topography with ^{10}Be catchment wide erosion rate and proposed tectonic uplift rate. Mean elevation and topographic relief were obtained from a swath profile parallel to the trace of the San Andreas Fault where topographic data were collected from lines perpendicular to the fault trace. The outline of the swath is on Fig. 4. Relief is defined as the range in elevation of topography. See text for discussion.

flooding events have a spatial distribution that is sufficient to cover all parts of the sampled catchment over the timescale of the measurement such that denudation is proportionately even. Second, we assume that the catchments in the Mecca Hills are small enough that when less frequent regional-scale storms occur, any heterogeneity of sediment provenance in channels is removed. Although it is hard to distinguish whether there is a local rather than catchment-averaged source for the samples due to the homogeneity of the sediment, we did not witness any field evidence to suggest that the samples are not representative of the catchment of interest. We may then explore the denudation rates as functions of geomorphic or tectonic variables.

We assume that precipitation and temperature variations do not contribute significantly to denudation rates based on previous research by von Blanckenburg (2005) and based on the uniform climate of the Mecca Hills. Furthermore, we reason that the extremely sparse vegetation in the Mecca Hills does not effectively anchor basin sediment to hillslopes. Because the applicable timespan for the majority of denudation rates is largely within the Holocene, and vegetation change may not have a large impact on sediment yield (Antinao and McDonald, 2013), this assumption is valid for the purpose of this study. Because the Mecca Hills is designated as a wilderness area, anthropogenic effects are limited to trail erosion which we also assume is minimal on catchment-wide scales. We also assume that controls on the relative denudation rate due to changes in lithology are minimal; the Mecca Hills is largely composed of the Palm Spring and Mecca Formations, which are composed of unlithified siliclastic sediment (Sylvester and Smith, 1976).

Table 7
Surface exposure ages for surfaces in the Mecca Hills.

Surface name	Age range (ka)	Weighted mean surface age (ka)	Depth profile age (ka)	Marine isotope stage (MIS)
Qvof1	200–475	266 ± 100	280 ± 24	MIS 8
Qvof2	11–160	67.2 ± 5.3 105 ± 11 29.5 ± 1.3	17.4 ± 6.1	MIS 4/5
Qyf1	3.8–17	8.2 ± 2.0	2.6 ± 5.55	MIS 1
Qt1	5.1–20	9.0 ± 4.8	–	MIS 1
Qac	5.1–40	8.4 ± 16	–	MIS 1

The comparison with geomorphic variables suggests that the influence of tectonics on denudation rates is significant (Figs. 9 and 10; Table 6) and potentially more important than any other tested variables. First, the relationships between geomorphic variables, catchment area, catchment mean elevation, and catchment total relief show no significant correlation (R^2 values of 0.03, 0.14, and 0.001, respectively). The lack of a relation between catchment size and denudation rate demonstrates that the variables are decoupled, and if a relationship between basin growth and denudation exists (Frankel and Pazzaglia, 2006), additional processes are acting on the catchments such that this relationship is obscured. Although basins at higher elevations generally are farther from base level and have high relief leading to higher denudation rates, this relationship is weak to nonexistent within our sampled catchments. This suggests that distance to relative base level may better explain the denudation rates which we test with the total catchment relief metric. One further consideration is that although major knickpoints in the stream systems have not been identified, the lack of correlation with variables may be suggesting that upper reaches of the drainage network have not yet responded to a transient signal of base level fall (Schumm, 1993; Reinhardt et al., 2007).

To test if the denudation rates are instead connected to the distance to relative base level, we compared the denudation rate to the total relief, defined as maximum minus minimum elevation within the catchment. We note that other researchers have defined catchment relief in other ways, most notably as a proxy for the average gradient within a basin. Here we prefer to use mean basin slope as a proxy for average gradient and total catchment relief as a

means of evaluating the vertical distance to relative base level. The correlation between catchment relief and erosion rate is the weakest among our tested geomorphic parameters (R^2 of 0.001), significantly lower than the global dataset regression (R^2 of 0.20; Portenga and Bierman, 2011). Catchment relief should positively influence denudation rates by increasing the amount of gravitational potential energy available to transport sediment.

Mean catchment slope demonstrated a notable correlation with denudation rate using a non-linear regression ($R^2 = 0.60$), consistent with the findings of other researchers (Roering et al., 1999; Binnie et al., 2007; Ouimet et al., 2009; DiBiase et al., 2010). The relatively strong correlation between denudation rate and catchment slope in the Mecca Hills may reflect a combination of the weakly indurated lithology of the Mecca Hills and steepening due to base level lowering from rapid tectonic uplift. In addition, shaking due to seismicity and rock weakening by tectonics stress may also play a role. Considerable work has been done exploring the connection between tectonic uplift, denudation rate, and mean basin slope (DiBiase et al., 2012, and references therein). It has been noted that above hillslope angle of repose thresholds (30–35°), denudation rates seem to no longer record tectonic information (DiBiase et al., 2010) although some work suggests otherwise (DiBiase et al., 2012). The mean slope angles for catchments in the Mecca Hills are all lower than the threshold ~30–35° (Table 4, Fig. 10) for the angle of repose for sand (Carrigy, 1970). Considering that the majority of sediment in the Mecca Hills is coarse to fine sand (Dibblee, 1954), this may suggest that hillslope failure is not common in the Mecca Hills. The adjustment of denudation rate with mean slope may then be more dependent on the diffusive downhill movement of grains. For a small range that is subjected to spatially uniform time-averaged precipitation, our observed denudation rates may be better explained by the diffusive movement of grains which may in turn be subjected to increased mobility from tectonic rock weakening and small-scale movement from seismic shaking.

As a proxy for tectonically induced rock weakening and seismic shaking, we evaluated the correlation between denudation rate and an index derived from the length of active faults within a catchment divided by total catchment area (Fig. 10, Table 6). This index demonstrated the greatest correlation of all variables tested against denudation rate ($R^2 = 0.85$; Table 6, Fig. 10) and suggests that this index may best describe the denudation rates in the Mecca Hills. We did not include samples from the Box Canyon drainage in the regression as these samples drain a catchment many times the size of the Mecca Hills and away from the areas of active uplift. Although correlation may not require causation, the strength of the correlation is compelling and we interpret the presence of fault lines as an indicator of greater rock weakening and local seismic shaking. These factors are thought to play a strong control on erosion via increasing rock 'erodibility' (Sklar et al., 2012), although this relationship represents a young research frontier. We interpret the strong correlation between our index with denudation rate as an indicator of rock weakening and shaking by tectonic forces which we in turn interpret as an indicator of greater rates of tectonic uplift. We support this interpretation with the correlation between rock uplift and denudation rate established by Gudmundsdottir et al. (2013) and conclude that our catchment-wide denudation rates are controlled to the greatest extent by tectonic variables and are therefore proportional proxies for tectonic uplift rates.

5.4. Landscape evolution

In the Mecca Hills, the maximum measured denudation rate occurs in Hidden Spring Wash (Figs. 4 and 11). In the first model (Model 1), the Mecca Hills is developed via a domal pattern where topographic growth and structural exhumation initiated near Painted Canyon and spread outwards, toward the northwest and southeast parallel along the San Andreas Fault (Fig. 2). Model 1 is supported by the greatest total exhumation observed at Painted Canyon where Orocopia Schist and related crystalline rocks are exposed (Sylvester and Smith, 1976) and the tapering of topography and exhumation away from the center of the range (Patt, 2000). In Model 1, uplift rates and erosion rates should have focal points on the edges of the spreading dome where the propagation of uplift alters the dynamic equilibrium of the landscape and produces high erosion rates on either side of the range (Hack, 1960; von Blankenberg, 2005). The tectonic uplift curve (Fig. 11) demonstrates a potential uplift pattern that supports Model 1 if fluvial incision rates reflect rock uplift rates rather than a climate-driven incision.

Alternatively, the Mecca Hills could be acting like the Dragon's Back pressure ridge and the Santa Cruz Mountains as examined by Hilley and Arrowsmith (2008) and Anderson (1990, 1994), respectively. Hilley and Arrowsmith (2008) proposed that topography and the erosional response along a small restraining bend, the Dragon's Back pressure ridge on the Carrizo Plain, can be explained by a focal point of rock uplift followed by advection of crust. This idea is also used to explain the topography of a much larger restraining bend in the San Andreas Fault, the Loma Prieta bend in the Santa Cruz Mountains by Anderson (1990, 1994). Hilley and Arrowsmith (2008) found that the greatest relief occurred after crust had been advected away from the focal point of maximum rock uplift rate. We use these findings to construct Model 2 which is based on a single focal point of uplift in which crustal material is uplifted while simultaneously being advected into and out of the uplifting zone (Fig. 2). This uplifting focal point could produce a rapid increase in denudation rate based on previously observed correlations of denudation rate with landscape rejuvenation (von Blanckenberg, 2005) and with rock exhumation patterns (Gudmundsdottir et al., 2013). If this were the case, we would expect a single point of high denudation rate at the northwestern end of the Mecca Hills followed by gradually lowering denudation rates towards the southwest as the landscape returns to pre-uplift equilibrium.

Our present data tentatively fit Model 1 and may better explain the currently measured topography and erosion rates across the Mecca Hills than Model 2. Key to this conclusion is the spatial distribution of denudation rates as evident in Fig. 11. Notably, the curve describing the spatial distribution of denudation rates has an apex at Hidden Spring Wash which asymmetrically tapers to lower values in the northwest and southeast. In Model 2, denudation rates should be highest at approximately 5000 m–75,000 m distance along the San Andreas Fault in Fig. 11 whereas Model 1 predicts that denudation rates should reach maxima at 5000–7500 m and 17,500–22,500 m (Hidden Spring Wash). Because denudation rates reach a maximum at Hidden Spring Wash, Model 1 is the best fit and the high denudation rate at Hidden Spring Wash represents the outward growth of the topography of the Mecca Hills. Even if sample MH-HG-ER1 were present, it would not be possible to explain the higher rates at Hidden Spring with a simple uplift and advection model. The geometry of the fault zone is such that a point of uplift or "structural knot" (Hilley and Arrowsmith, 2008) would have to be fixed to the Pacific plate and generating uplift in the NW region of the Mecca Hills and the denudation rates would have to decline to the southwest as the landscape returns to pre-uplift equilibrium. It is possible that Model 1 could accommodate any potential value of MH-HG-ER1 by allowing domal growth to occur asymmetrically such that either side of the growth could be occurring faster or slower than the other side. This would produce a

range of denudation rate curves, but would still favor Model 1. The "tectonic uplift curve" on Fig. 11 circumstantially supports Model 1. However, because this curve combines uplift rates of different temporal scales this curve is a first-order approximation and is not necessarily conclusive of the actual uplift pattern.

The support of Model 1 from our data points toward a growth pattern that marks a sudden shift toward convergence that initiated the growth of the Mecca Hills in a manner consistent with the findings of previous researchers (Sylvester and Smith, 1976). Although the models presented here do not directly model fault dynamics, they imply favored conditions of deformation which may in turn provide constraints toward understanding the development of the southern San Andreas Fault. One potential implication of our favored model, Model 1, is that a sudden shift from a strike slip system to oblique convergence may have occurred on the southern San Andreas Fault in order to generate the uplift responsible for the Mecca Hills. Further research in the initiation of uplift in the Indio and Durmid Hills to the north and south of the Mecca Hills may provide evidence for changes in fault dynamics across the southern San Andreas Fault zone and help interpret the consequences of the initiation of the San Jacinto Fault zone.

Furthermore, the results presented here and the relative success of Model 1 in predicting the Quaternary topographic development of the Mecca Hills has implications for understanding the evolution of restraining bends. First, the Mecca Hills presents a useful real-world comparison to analog and numerical models of restraining bend development (McClay and Bonora, 2001; Li et al., 2009; Cooke et al., 2013). In particular, the focus on the topographic and denudational relationships at this scale complements efforts to understand the increasingly complex nature of these systems (Marques and Cobbold, 2002; Cowgill et al., 2004; Cunningham, 2007; Cruz et al., 2010; Leever et al., 2011; Cooke et al., 2013). Whereas much attention is given to the development of fault systems and uplift patterns over the past decade (Cooke et al., 2013 and references therein), understanding the influence of topographic and denudational variables on Quaternary and older restraining bends remains a significant goal (Anderson, 1990; Cunningham and Mann, 2007) and this study attempts to provide further work toward it. Second, the use of ^{10}Be catchment-wide denudation rates to infer uplift patterns is a very recent methodological advance (Gudmundsdottir et al., 2013) and this study represents one of the first attempts at its application. Uncovering the patterns of uplift in restraining bends in other strike-slip systems such as the Dead Sea fault system (Gomez et al., 2007), Mongolian Altai (Cunningham, 2007), Alpine fault system in New Zealand (Little et al., 2005) and many others distributed globally (Mann, 2007) may help test models of their tectonic development. This study, paired with prior and future work, will help evaluate the utility of this new tool and hopefully assist other researchers in its application.

6. Conclusions

The Mecca Hills is a result of Quaternary sedimentation, denudation, and tectonic deformation that has produced distinct landforms and varied catchment geometries. We developed and tested two models for the formation of the Mecca Hills based on previous research on the morphologic development of restraining bends. The implications of these models contribute to our knowledge of the evolution of the southern San Andreas Fault, a key structure in the Pacific–North American plate boundary. We tested our models using (1) geomorphic mapping with an emphasis on alluvial fans; (2) ^{10}Be geochronology to assess ages and fluvial incision rates of geomorphic surfaces (Table 7); and (3) measurement of ^{10}Be in sediment to quantify catchment-averaged rates of denudation to evaluate tectonic uplift patterns. Beryllium-10 surface exposure geochronology yields alluvial fan surface ages of 266 ± 100 ka for surface Qvof1, 69.5 ± 3.5 ka for surface Qvof2, and 8.2 ± 2.1 ka for surface Qyf1. Depth profiles reveal surface exposure ages of 280 ± 24 ka for surface Qvof1, 17.4 ± 6.1 ka for surface Qvof2, and 2.6 +5.6/−1.3 ka for Qyf1. Differences in depth profile and boulder surface exposure ages are likely the result of surface erosion, inheritance of ^{10}Be, and the possible recycling of older alluvial fan material. Surfaces Qyf1 and Qvof2 correlate with probability peaks in regional compilations (Owen et al., 2014). Denudation rates taken from catchments in the Mecca Hills range from 19.9 ± 3.2 m/Ma in the NW border of the Mecca Hills to 149.7 ± 22.5 m/Ma in Hidden Spring Wash (Table 5).

The strong correlation between mean catchment slope and total fault length normalized by catchment area, and the weak to no correlation with other geomorphic variables, suggest a coupling between denudation and local tectonic uplift. We interpret the spatial patterns of denudation as a proxy for the patterns of uplift rate following Gudmundsdottir et al. (2013). Following this, we find that a model based on a domal radial growth of topography (Model 1, Fig. 2) best describes the growth of the topography of the Mecca Hills. Consequently, the growth of the Mecca Hills may not be due to a fault plane heterogeneity or "structural knot" (Hilley and Arrowsmith, 2008). This growth pattern of the Mecca Hills has implications for the dynamics of the San Andreas Fault and since the uplift would not be due to a local heterogeneity. We hypothesize that a change in the stress field on the San Andreas Fault occurred after the initiation of the nearby San Jacinto Fault at 1.0–1.1 Ma. Further research on the evolution of the Indio Hills to the north and Durmid hill to the south may provide a way to further test this hypothesis.

Acknowledgements

This paper is dedicated to the memory of Professor Kurt Frankel. We would like to thank Susan Ma, and the staff at PRIME lab, Purdue University, for performing AMS measurements of ^{10}Be, and to CAMS at Lawrence Livermore National Laboratory. Thank you to Sarah Trischler, Rebecca Potter, and Kathryn Hedrick at the University of Cincinnati for help with sample preparation, and to Jeanette Arkle, Rebecca Potter, Suyoung Lee (especially for use of her photographs), and Miles Kenney for field assistance. LAO would like to thank Gary Patt for stimulating discussion in the Mecca Hills. We are grateful to two anonymous reviewers who substantially improved early versions of the manuscript. Any use of trade, product, or firm names is for descriptive purposes only and does not imply endorsement by the U.S. Government.

Appendix A. Supplementary data

Supplementary data related to this article can be found at http://dx.doi.org/10.1016/j.quascirev.2014.09.009.

References

Amit, R., Gerson, R., Yaalon, D.H., 1993. Stages and rate of the gravel shattering process by salts in desert Reg soils. Geoderma 57 (3), 44–56.
Anderson, R.S., 1990. Evolution of the northern Santa Cruz Mountains by advection of crust past a San Andreas fault bend. Science 249 (4967), 397–401.
Anderson, R.S., 1994. Evolution of the Santa Cruz Mountains, California, through tectonic growth and geomorphic decay. J. Geophys. Res. Solid Earth (1978–2012) 99 (B10), 20161–20179.
Anderson, Robert S., Repka, James L., Dick, Gregory S., 1966. Explicit treatment of inheritance in dating depositional surfaces using in situ 10Be and 26Al. Geology 24, 47–51.
Antinao, J.L., McDonald, E., 2013. An enhanced role for the Tropical Pacific on the humid Pleistocene–Holocene transition in southwestern North America. Quat. Sci. Rev. 78, 319–341.

Axen, Gary J., Fletcher, John M., 1998. Late Miocene-Pleistocene extensional faulting, northern gulf of California, Mexico and salton trough, California. Int. Geol. Rev. 40 (3), 217–244.
Aydin, A., Johnson, A.M., Fleming, R.W., 1992. Right-lateral-reverse surface rupture along the San Andreas and Sargent faults associated with the October 17, 1989, Loma Prieta, California, earthquake. Geology 20, 1063.
Balco, G., 2009. MATLAB Code for Camel Diagrams. http://cosmognosis.wordpress.com/2009/07/13/matlab-code-for-camel-diagrams (February 2013).
Balco, G., Shuster, D.L., 2009. 26Al–10 Be– 21Ne burial dating. Earth Planet. Sci. Lett. 286 (3), 570–575.
Balco, G., Stone, J.O., Lifton, N.A., Dunai, T.J., 2008. A complete and easily accessible means of calculating surface exposure ages or erosion rates from10Be and 26Al measurements. Quat. Geochronol. 3 (3), 174–195.
Behr, W.M., Rood, D.H., Fletcher, K.E., Guzman, N., Finkel, R., Hanks, T.C., Hudnut, K.W., Kendrick, K.J., Platt, J.P., Sharp, W.D., Weldon, R.J., Yule, J.D., 2010. Uncertainties in slip-rate estimates for the Mission Creek strand of the southern San Andreas fault at Biskra Palms Oasis, southern California. Geol. Soc. Am. Bull. http://dx.doi.org/10.1130/B30020.1. B30020.1, first published on May 10, 2010.
Bennett, R.A., Friedrich, A.M., Furlong, K.P., 2004. Codependent histories of the San Andreas and San Jacinto fault zones from inversion of fault displacement rates. Geology 32 (11), 961–964.
Bevis, M., Hudnut, K., Sanchez, R., Toth, C., Grejner-Brzezinska, D., Kendrick, E., Caccamise, D., Raleigh, D., Zhou, H., Shan, S., Shindle, W., Yong, A., Harvey, J., Borsa, A., Ayoub, F., Elliot, B., Shrestha, R., Carter, B., Sartori, M., Phillips, D., Coloma, F., Stark, K., 2005. The B4Project: scanning the San Andreas and San Jacinto fault zones. Eos Trans AGU 86 (52). Fall Meet Suppl, Abstract H34B-01.
Bierman, P.R., Steig, E., 1996. Estimating rates of denudation and sediment transport using cosmogenic isotope abundances in sediment. Earth Surf. Process. Landf. 21, 125–139.
Bilham, R., Williams, P., 1985. Sawtooth segmentation and deformation processes on the southern San Andreas fault, California. Geophys. Res. Lett. 12 (9), 557–560.
Binnie, S.A., Phillips, W.M., Summerfield, M.A., Fifield, L.K., 2007. Tectonic uplift, threshold hillslopes, and denudation rates in a developing mountain range. Geology 35 (8), 743–746.
Binnie, S.A., Phillips, W.M., Summerfield, M.A., Fifield, L.K., Spotila, J.A., 2008. Patterns of denudation through time in the San Bernardino Mountains, California: implications for early-stage orogenesis. Earth Planet. Sci. Lett. 276 (1–2), 62–72.
Blisniuk, K., Oskin, M., Fletcher, K., Rockwell, T., Sharp, W., 2012. Assessing the reliability of U-series and 10Be dating techniques on alluvial fans in the Anza Borrego Desert, California. Quat. Geochronol.
Boley, J.L., Stimac, J.P., Weldon, R.J., Rymer, M.J., 1994. Stratigraphy and Paleomagnetism of the Mecca and Indio Hills, southern California. In: McGill, S.F., Ross, T.M. (Eds.), Geological Investigations of an Active Margin, G.S.A. Cordilleran Section Guidebook, Trip 15, pp. 336–344.
Briner, J.P., Young, N.E., Goehring, B.M., Schaefer, J.M., 2012. Constraining Holocene 10Be production rates in Greenland. J. Quat. Sci. 27, 2–6.
Brothers, D.S., Driscoll, N.W., Kent, G.M., Harding, A.J., Babcock, J.M., Baskin, R.L., 2009. Tectonic evolution of the Salton Sea inferred from seismic reflection data. Nat. Geosci. 2 (8), 581–584.
Brown, E.T., Stallard, R.F., Larsen, M.C., Raisbeck, G.M., Yiou, F., 1995. Denudation rates determined from the accumulation of in situ-produced ^{10} Be in the Luquillo experimental forest, Puerto Rico. Earth Planet. Sci. Lett. 129 (1), 193–202.
Bull, W.B., 1991. Geomorphic Responses to Climate Change. Oxford University Press, New York.
Bull, W.B., 2000. Correlation of fluvial aggradation events to times of global climate change. In: Noller, J.S., Sowers, J.M., Lettis, W.R. (Eds.), Quaternary Geochronology: Methods and Applications. American Geophysical Union, Washington, D.C, pp. 456–464.
Bull, W.L., Knuepfer, P.L., 1987. Adjustments by the Charwell River, New Zealand, to uplift and climatic changes. Geomorphology 1 (1), 15–32.
Burbank, D.W., Anderson, R.S., 2011. Tectonic Geomorphology. Wiley.com.
Bürgmann, R., Arrowsmith, R., Dumitru, T., McLaughlin, R., 1994. Rise and fall of the southern Santa Cruz Mountains, California, from fission tracks, geomorphology, and geodesy. J. Geophys. Res. Solid Earth (1978–2012) 99 (B10), 20181–20202.
Burke, R.M., Birkeland, P.W., 1979. Reevaluation of multiparameter relative dating techniques and their application to the glacial sequence along the eastern escarpment of the Sierra Nevada, California. Quat. Res. 11 (1), 21–51.
Carrigy, M.A., 1970. Experiments on the angles of repose of granular materials. Sedimentology 14 (3–4), 147–158.
Chang, S.B.R., Allen, C.R., Kirschvink, J.L., 1987. Magnetic stratigraphy and a test for block rotation of sedimentary rocks within the San Andreas fault zone, Mecca Hills, southeastern California. Quat. Res. 27 (1), 30–40.
Cooke, M.L., Schottenfeld, M.T., Buchanan, S.W., 2013. Evolution of fault efficiency at restraining bends within wet kaolin analog experiments. J. Struct. Geol. 51, 180–192.
Cowgill, E., Yin, A., Arrowsmith, J.R., Feng, W.X., Shuanhong, Z., 2004. The Akato Tagh bend along the Altyn Tagh fault, northwest Tibet 1: smoothing by vertical-axis rotation and the effect of topographic stresses on bend-flanking faults. Geol. Soc. Am. Bull. 116 (11–12), 1423–1442.
Crowley, J.L., Schoene, B., Bowring, S.A., 2007. U-Pb dating of zircon in the Bishop Tuff at the millennial scale. Geology 35 (12), 1123–1126.
Cruz, L., Malinski, J., Wilson, A., Take, W.A., Hilley, G., 2010. Erosional control of the kinematics and geometry of fold-and-thrust belts imaged in a physical and numerical sandbox. J. Geophys. Res. Solid Earth (1978–2012) 115 (B9).
Cyr, A.J., Granger, D.E., Olivetti, V., Molin, P., 2010. Quantifying rock uplift rates using channel steepness and cosmogenic nuclide–determined erosion rates: Examples from northern and southern Italy. Lithosphere 2 (3), 188–198.
Cunningham, D., 2007. Structural and Topographic Characteristics of Restraining Bend Mountain Ranges of the Altai, Gobi Altai and Easternmost Tien Shan. In: Geological Society, London, Special Publications, 290, pp. 219–237.
Cunningham, W.D., Mann, P., 2007. Tectonics of Strike-slip Restraining and Releasing Bends. In: Geological Society, London, Special Publications, vol. 290(1), pp. 1–12.
Dibblee Jr., T.W., 1954. Geology of the Imperial Valley region, California. Geol. South. Calif. Calif. Div. Mines Bull. 170, 21–28.
DiBiase, R., Whipple, K., Heimsath, A., Ouimet, W., 2010. Landscape form and millennial erosion rates in the San Gabriel Mountains, CA. Earth Planet. Sci. Lett. 289 (1–2), 134–144.
DiBiase, R.A., Heimsath, A.M., Whipple, K.X., 2012. Hillslope response to tectonic forcing in threshold landscapes. Earth Surf. Process. Landf. 37 (8), 855–865.
Dorsey, R.J., Axen, G.J., Peryam, T.C., Kairouz, M.E., 2012. Initiation of the southern Elsinore fault at ~1.2 Ma: evidence from the Fish Creek – Vallecito Basin, southern California. Tectonics 31, TC2006. http://dx.doi.org/10.1029/2011TC003009.
Dortch, J.M., Owen, L.A., Schoenbohm, L.M., Caffee, M.W., 2011. Asymmetrical erosion and morphological development of the central Ladakh Range, northern India. Geomorphology 135 (1), 167–180.
Fattaruso, L., Cooke, M.L., Dorsey, R.J., 2013. Mechanical insights into tectonic reorganization of the southern San Andreas fault system at ca. 1.1–1.5 Ma. In: AGU Fall Meeting Abstracts, vol. 1, p. 2482.
Fossen, H., Tikoff, B., 1998. Extended Models of Transpression and Transtension, and Application to Tectonic Settings. In: Geological Society, London, Special Publications, vol. 135(1), pp. 15–33.
Frankel, K.L., Pazzaglia, F.J., 2006. Mountain Fronts, Base-level Fall, and Landscape Evolution: Insights from the Southern Rocky Mountains. Special Papers-Geological Society of America 398, 419.
Frankel, K.L., Finkel, R.C., Owen, L.A., 2010. Terrestrial cosmogenic nuclide geochronology data reporting standards needed. Eos Trans. Am. Geophys. Union 91 (4), 31–32.
Gesch, D.B., 2007. The National Elevation Dataset. In: Maune, D. (Ed.), Digital Elevation Model Technologies and Applications: The DEM Users Manual, 2nd Edition. American Society for Photogrammetry and Remote Sensing, Bethesda, Maryland, pp. 99–118.
Gesch, D., Oimoen, M., Greenlee, S., Nelson, C., Steuck, M., Tyler, D., 2002. The National Elevation Dataset. Photogrammetric Engineering and Remote Sensing 68 (1), 5–11.
Gosse, J.C., Phillips, F.M., 2001. Terrestrial in situ cosmogenic nuclides: theory and application. Quaternary Science Reviews 20 (14), 1475–1560.
Gomez, F., Karam, G., Khawlie, M., McClusky, S., Vernant, P., Reilinger, R., Jaafar, R., Tabet, C., Khair, K., Barazangi, M., 2007. Global Positioning System measurements of strain accumulation and slip transfer through the restraining bend along the Dead Sea fault system in Lebanon. Geophysical Journal International 168 (3), 1021–1028.
Granger, D.E., Kirchner, J.W., Finkel, R., 1996. Spatially averaged long-term erosion rates measured from in situ-produced cosmogenic nuclides in alluvial sediments. J. Geol. 104 (3), 249–257.
Gudmundsdottir, M.H., Blisniuk, K., Ebert, Y., Levine, N.M., Rood, D.H., Wilson, A., Hilley, G.E., 2013. Restraining bend tectonics in the Santa Cruz Mountains, California, imaged using 10Be concentrations in river sands. Geology 41 (8), 843–846.
Hack, J., 1960. Interpretation of erosional topography in humid temperate regions. Am. J. Sci. 258-A, 80–97.
Harvey, A.M., Wigand, P.E., Wells, S.G., 1999. Response of alluvial fan systems to the late Pleistocene to Holocene climatic transition: contrasts between the margins of pluvial Lakes Lahontan and Mojave, Nevada and California, USA. Catena 36 (4), 255–281.
Hays, W.H., 1957. Geology of the Central Mecca Hills, Riverside County, California. Yale University, p. 324. PhD dissertation.
Hidy, Alan J., et al., 2010. A geologically constrained Monte Carlo approach to modeling exposure ages from profiles of cosmogenic nuclides: an example from Lees Ferry, Arizona. Geochem. Geophys. Geosyst. 11 (9).
Hilley, G.E., Arrowsmith, J.R., 2008. Geomorphic response to uplift along the Dragon's Back pressure ridge, Carrizo Plain, California. Geology 36 (5), 367–370.
Hooke, R.LeB., Dorn, R.I., 1992. Segmentation of alluvial fans in Death Valley, California- new insights from surface-exposure dating and laboratory modeling. Earth Surf. Process. Landf. 17, 57–574.
Izett, G.A., Naeser, C.W., 1976. Age of the Bishop Tuff of eastern California as determined by the fission-track method. Geology 4 (10), 587–590.
Janecke, S.U., Dorsey, R.J., Steely, A.N., Kirby, S.M., Lutz, A.T., Housen, B.A., Belgarde, B., Langenheim, V., Rittenour, T., Forand, D., 2010. High Geologic Slip Rates Since Early Pleistocene Initiation of the San Jacinto and San Felipe Fault Zones in the San Andreas Fault System: Southern California, USA. Geological Society America Special Paper 475, 48.
Kirby, E., Whipple, K., Harkins, N., 2008. Topography reveals seismic hazard. Nat. Geosci. 1 (8), 485–487.
Lal, D., 1991. Cosmic ray labeling of erosion surfaces: in situ nuclide production rates and erosion models. Earth Planet. Sci. Lett. 104 (2), 424–439.
Lal, D., Arnold, J.R., 1985. Tracing quartz through the environment. In: Proceedings of the Indian Academy of Sciences-earth and Planetary Sciences, vol. 94(1), pp. 1–5.

Lancaster, N., 1984. Characteristics and occurrence of wind erosion features in the Namib Desert. Earth Surf. Process. Landf. 9, 469–478. http://dx.doi.org/10.1002/esp.3290090507.
Leever, K.A., Gabrielsen, R.H., Sokoutis, D., Willingshofer, E., 2011. The effect of convergence angle on the kinematic evolution of strain partitioning in transpressional brittle wedges: insight from analog modeling and high-resolution digital image analysis. Tectonics 30 (2).
Li, Q., Liu, M., Zhang, H., 2009. A 3-D viscoelastoplastic model for simulating long-term slip on non-planar faults. Geophys. J. Int. 176 (1), 293–306.
Lifton, N., Caffee, M.W., Finkel, R., Schaefer, J.M., Stone, J., Goehring, B.M., Oviatt, Charles, Rood, D.H., 2009. A new estimate of the spallogenic production rate of in situ cosmogenic 10 Be from Lake Bonneville Shoreline features, promontory point, Utah. In: 2009 Portland GSA Annual Meeting.
Lisiecki, L.E., Raymo, M.E., 2005. A Pliocene-Pleistocene stack of 57 globally distributed benthic δ18O records. Paleoceanography 20 (1).
Litchfield, N., Berryman, K., 2006. Relations between postglacial fluvial incision rates and uplift rates in the North Island, New Zealand. J. Geophys. Res. Earth Surf. (2003–2012) 111 (F2).
Little, T.A., Cox, S., Vry, J.K., Batt, G., 2005. Variations in exhumation level and uplift rate along the obliqu-slip Alpine fault, central Southern Alps, New Zealand. Geol. Soc. Am. Bull. 117 (5–6), 707–723.
Mann, P., 2007. Global Catalogue, Classification and Tectonic Origins of Restraining- and Releasing Bends on Active and Ancient Strike-slip Fault Systems. In: Geological Society, London, Special Publications, vol. 290(1), pp. 13–142.
Marques, F.O., Cobbold, P.R., 2002. Topography as a major factor in the development of arcuate thrust belts: insights from sandbox experiments. Tectonophysics 348 (4), 247–268.
MATLAB v, 2009. Matrix Laboratory — the Language of Technical Computing. http://www.mathworks.com/.
Matmon, Ari, et al., 2009. Desert pavement–coated surfaces in extreme deserts present the longest-lived landforms on Earth. Geol. Soc. Am. Bull. 121 (5–6), 688–697.
McClay, K., Bonora, M., 2001. Analog models of restraining stepovers in strike-slip fault systems. AAPG bulletin 85 (2), 233–260.
McDougall, I., Harrison, T.M., 1988. Geochronology and Thermochronology by the 40Ar/39Ar Method. Oxford University Press.
McFadden, L.D., Ritter, J.B., Wells, S.G., 1989. Use of multiparameter relative-age methods for age estimation and correlation of alluvial fan surfaces on a desert piedmont, eastern Mojave Desert, California. Quat. Res. 32 (3), 276–290.
McNabb, J., Dorsey, R., 2012. Stratigraphic record of vertical crustal motions in the past 2-3 Ma along the Coachella Valley segment of the San Andreas fault, Mecca Hills, California. In: Southern California Earthquake Center Annual Meeting. Palm Springs, CA, Poster.
McNabb, J.C., Dorsey, R.J., Housen, B.A., Messe, G.T., 2013 December. Stratigraphic record of Basin formation, deformation, and destruction in the past 2 ma along the southern San Andreas fault, Mecca Hills, California. In: AGU Fall Meeting Abstracts, vol. 1, p. 2484.
Merriam, R., Bischoff, J.L., 1975. Bishop Tuff; a widespread volcanic ash extended to southern California. J. Sediment. Res. 45 (1), 207–211.
Miller, D.M., Schmidt, K.M., Mahan, S.A., McGeehin, J.P., Owen, L.A., Barron, J.A., Lehmkuhl, F., Löhrer, R., 2010. Holocene landscape response to seasonality of storms in the Mojave Desert. Quat. Int. 215 (1), 45–61.
Morton, D.M., Matti, J.C., 1993. Extension and Contraction Within an Evolving Divergent Strike-Slip Fault Complex: The San Andreas and San Jacinto Fault Zones at Their Convergence in Southern California. In: Powell, R.E., Weldon, R.J., Matti, J.C. (Eds.), The San Andreas Fault System: Displacement, Palinspastic Reconstruction,and Geologic Evolution, vol. 178. Geological Society of America, Memoir, pp. 217–230.
Nishiizumi, K., Kohl, C.P., Arnold, J.R., Dorn, R., Klein, I., Fink, D., Lal, D., 1993. Role of in situ cosmogenic nuclides 10Be and 26Al in the study of diverse geomorphic processes. Earth Surf. Process. Landf. 18 (5), 407–425.
Ouimet, W.B., Whipple, K.X., Granger, D.E., 2009. Beyond threshold hillslopes: channel adjustment to base-level fall in tectonically active mountain ranges. Geology 37 (7), 579–582.
Owen, L.A., Finkel, R.C., Minnich, R.A., Perez, A.E., 2003. Extreme southwestern margin of late Quaternary glaciation in North America: timing and controls. Geology 31 (8), 729–732.
Owen, L.A., Frankel, K.L., Knott, J.R., Reynhout, S., Finkel, R.C., Dolan, J.F., Lee, J., 2011. Beryllium-10 terrestrial cosmogenic nuclide surface exposure dating of Quaternary landforms in Death Valley. Geomorphology 125 (4), 541–557.
Owen, L., Clemmens, S.J., Finkel, R.C., Gray, H., 2014. Late Quaternary alluvial fans at the eastern end of the San Bernardino Mountains, Southern California. Quat. Sci. Rev. 87, 114–134.
Patt, G., 2000. The Tectonic Geomorphology of the Mecca Hills: a Young Transpressional Mountain Range. Master's thesis. University of California, Riverside, 85 pp.
Petersen, M.D., et al., 2008. United States National Seismic Hazard Maps. U.S. Geological Survey Fact Sheet 2008–3017, 4 p.
Philip, H., Meghraoui, M., 1983. Structural analysis and interpretation of the surface deformations of the El Asnam earthquake of October 10, 1980. Tectonics 2, 17–49. http://dx.doi.org/10.1029/TC002i001p00017.
Portenga, E.W., Bierman, P.R., 2011. Understanding Earth's eroding surface with 10 Be. GSA Today 21 (8), 4–10.
Powell, R., Hergt, J., Woodhead, J., 2002. Improving isochron calculations with robust statistics and the bootstrap. Chem. Geol. 185, 191–204.
Putkonen, Jaakko, Swanson, Terry, 2003. Accuracy of cosmogenic ages for moraines. Quat. Res. 59 (2), 255–261.
Reid, M.R., Coath, C.D., 2000. In situ U-Pb ages of zircons from the Bishop Tuff: no evidence for long crystal residence times. Geology 28 (5), 443–446.
Reinhardt, L.J., Bishop, P., Hoey, T.B., Dempster, T.J., Sanderson, D.C.W., 2007. Quantification of the transient response to base-level fall in a small mountain catchment: Sierra Nevada, southern Spain. J. Geophys. Res. Earth Surf. (2003–2012) 112 (F3).
Ritter, J.B., Miller, J.R., Enzel, Y., Wells, S.G., 1995. Reconciling the roles of tectonism and climate in Quaternary alluvial fan evolution. Geology 23 (3), 245–248.
Rodés, Á., Pallàs, R., Braucher, R., Moreno, X., Masana, E., Bourlés, D.L., 2011. Effect of density uncertainties in cosmogenic 10Be depth-profiles: dating a cemented Pleistocene alluvial fan (Carboneras Fault, SE Iberia). Quat. Geochronol. 6 (2), 186–194.
Roering, J.J., Kirchner, J.W., Dietrich, W.E., 1999. Evidence for nonlinear, diffusive sediment transport on hillslopes and implications for landscape morphology. Water Resources Research 35 (3), 853–870.
Rymer, M.J., 1991. Geologic Structure, Transpression, and Neotectonics of the San Andreas Fault in the Salton Trough, California; Part 2, the Bishop Tuff in the Mecca Hills. In: Geological Excursions in Southern California and Mexico. San Diego State Univ, San Diego, CA, pp. 388–396.
Schumm, S.A., 1993. River response to baselevel change: implications for sequence stratigraphy. J. Geol. 279–294.
Sklar, L.S., Beyeler, J.D., Collins, G.C., Farrow, J.W., Hsu, L., Litwin, K.L., Polito, P.J., 2012. Laboratory experiments for defining scaling relations between rock material properties and rock resistance to erosion. In: AGU Fall Meeting Abstracts, vol. 1, p. 08.
Spelz, R.M., Fletcher, J.M., Owen, L.A., Caffee, M.W., 2008. Quaternary alluvial-fan development, climate and morphologic dating of fault scarps in Laguna Salada, Baja California, Mexico. Geomorphology 102 (3), 578–594.
Spotila, J.A., House, M.A., Niemi, N.A., Brady, R.C., Oskin, M., Buscher, J.T., 2007. Patterns of Bedrock Uplift Along the San Andreas Fault and Implications for Mechanisms of Transpression. Special Papers-Geological Society of America 434, p. 15.
State of California, 2013. Cal –Atlas, Geospatial Clearinghouse. http://atlas.ca.gov/ (June, 2013).
Stone, J.O., 2000. Air pressure and cosmogenic isotope production. J. Geophys. Res. 105 (B10), 23753–23823.
Streule, M.J., Phillips, R.J., Searle, M.P., Waters, D.J., Horstwood, M.S.A., 2009. Evolution and chronology of the Pangong Metamorphic Complex adjacent to the Karakoram Fault, Ladakh: constraints from thermobarometry, metamorphic modelling and U-Pb geochronology. J. Geol. Soc. 166, 919–932. http://dx.doi.org/10.1144/0016-76492008-117.
Sylvester, A.G., 1988. Strike-slip faults. Geol. Soc. Am. Bull. 100 (11), 1666–1703.
Sylvester, A.G., Smith, R.R., 1976. Tectonic transpression and basement-controlled deformation in San Andreas fault zone, Salton Trough, California. AAPG Bull. 60 (12), 2081–2102.
U.S. Geological Survey and California Geological Survey, 2013. Quaternary fault and fold database for the United States. http//earthquakes.usgs.gov/regional/qfaults/ (accessed June 2013).
Van der Woerd, J., Klinger, Y., Sieh, K., Tapponnier, P., Ryerson, F.J., Mériaux, A.S., 2006. Long-term slip rate of the southern San Andreas fault from 10Be–26Al surface exposure dating of an offset alluvial fan. J. Geophys. Res. Solid Earth (1978–2012) 111 (B4).
von Blanckenburg, F., 2005. The control mechanisms of erosion and weathering at basin scale from cosmogenic nuclides in river sediment. Earth Planet. Sci. Lett. 237 (3), 462–479.
Ware, G.C., 1958. The Geology of a Portion of the Mecca Hills, Riverside County, California. University of California, Los Angeles, p. 60. Master's thesis.
Wells, S.G., Harvey, A.M., 1987. Sedimentologic and geomorphic variations in storm-generated alluvial fans, Howgill Fells, northwest England. Geol. Soc. Am. Bull. 98 (2), 182–198.
Wells, S.G., McFadden, L.D., Dohrenwend, J.C., 1987. Influence of late Quaternary climatic changes on geomorphic and pedogenic processes on a desert piedmont, eastern Mojave Desert, California. Quat. Res. 27, 130–146.
Wells, S.G., McFadden, L.D., Harden, J., 1990. Preliminary results of age estimations and regional correlations of Quaternary alluvial fans within the Mojave Desert of Southern California. In: Reynolds, R.E., Wells, S.G., Brady, R.J.I. (Eds.), At the End of the Mojave: Quaternary Studies in the Eastern Mojave Desert. Special publications of the San Bernardino County Museum Association, Redlands, CA, pp. 45–53.
Wobus, C., Whipple, K.X., Kirby, E., Snyder, N., Johnson, J., Spyropolou, K., Crosby, B., Sheehan, D., 2006. Tectonics from topography: procedures, promise, and pitfalls. Special Papers-Geol. Soc. Am. 398, 55–65.
Woodcock, N.H., Fischer, M., 1986. Strike-slip duplexes. J. Struct. Geol. 8 (7), 725–735.